BNL - 62331
Interim Report

SYNTHESIS AND CHARACTERIZATION OF METAL HYDRIDE ELECTRODES

J. McBreen and J. J. Reilly

October 1995

Research Supported by the
DIVISION OF CHEMICAL SCIENCES
UNITED STATES DEPARTMENT OF ENERGY

Chemical Sciences Division
DEPARTMENT OF APPLIED SCIENCE

BROOKHAVEN NATIONAL LABORATORY
UPTON, LONG ISLAND, NEW YORK 11973

SYNTHESIS AND CHARACTERIZATION OF METAL HYDRIDE ELECTRODES

INTERIM REPORT

Principal Investigators

James McBreen and James J. Reilly

Contributors

S. Mukerjee **G. Adzic**

J. R. Johnson

October 1995

Research Supported by the
DIVISION OF CHEMICAL SCIENCES
UNITED STATES DEPARTMENT OF ENERGY

CHEMICAL SCIENCES DIVISION
DEPARTMENT OF APPLIED SCIENCE
BROOKHAVEN NATIONAL LABORATORY
UPTON, NEW YORK 11973
Under Contract No. DE-AC02-76CH00016 with the
UNITED STATES DEPARTMENT OF ENERGY

TABLE OF CONTENTS

SUMMARY

The objective of this project is to elucidate the compositional and structural parameters that affect the thermodynamics, kinetics and stability of alloy hydride electrodes and to use this information in the development of new high capacity long life hydride electrodes for rechargeable batteries. The work focuses on the development of AB_5 alloys and the application of *in situ* methods, at NSLS, such as x-ray absorption (XAS), to elucidate the role of the alloying elements in hydrogen storage and corrosion inhibition. The most significant results to date are:

- The decay of electrode capacity on cycling was directly related to alloy corrosion.
- The rate of corrosion depended in part on both the alloy composition and the partial molar volume of hydrogen, V_H.
- The corrosion rate depended on the composition of the A component in AB_5 ($LaNi_5$ type) alloys.
- Partial substitution of La with Ce in AB_5 alloys substantially inhibits electrode corrosion on cycling.
- Recent results indicate that Co also greatly inhibits electrode corrosion, possibly by minimizing V_H.

The AB_5 alloys investigated included $LaNi_5$, ternary alloys (e.g. $LaNi_{4.8}Sn_{0.2}$ and $La_{0.8}Ce_{0.2}Ni_5$), alloys with various substitutions for both La and Ni (e.g. $La_{0.8}Ce_{0.2}Ni_{4.8}Sn_{0.2}$) and mischmetal (Mm) alloys of the type normally used in batteries, such as MmB_5 (B = $Ni_{3.55}Mn_{0.4}Al_{0.3}Co_{0.75}$). A major effort was devoted to the effects of La substitution in the A component. Almost all the alloys were prepared at BNL by arc melting and were characterized by x-ray diffraction and by hydrogen absorption measurements in a Sieverts apparatus. The partial molar volume of hydrogen in many of the alloys was determined by x-ray diffraction. Materials that had plateau pressures below one atmosphere were fabricated into electrodes and were cycled in cells to determine electrode performance and stability with cycling. It was found that the loss of electrochemical capacity per charge-discharge cycle, due to electrode corrosion, was significantly decreased by the presence of Ce in the alloy. XAS was used to follow the corrosion of individual elements on cycling. In the case of Ni quantitative determinations could be made of the degree of corrosion. A direct relationship was found between capacity loss and Ni corrosion. The XAS results showed considerably reduced Ni corrosion in Ce containing alloys. The scanning vibrating electrode technique (SVET) was used to monitor corrosion of alloy ingots at potentials positive to the reversible hydriding potential. These measurements also confirmed the corrosion inhibiting effect of Ce.

Both *in situ* and *ex situ* XAS measurements are used to study the electronic effects that occur on the addition of various metal substitutions and on the ingress of hydrogen. The results indicate

that XAS is a very useful technique for the study of alloy hydrides, particularly the role of electronic structure, the environment around minor constituents, and the corrosion of individual components. The x-ray absorption near edge fine structure (XANES) results at the Ni K edge indicates that the alloying process results in hybridization of the $4p$ and $3d$ orbitals of Ni. The addition of Sn and Ce apparently decreases the number of Ni d band vacancies. This could account for both the decrease hydrogen content and the reduced plateau pressure. All of the XANES results at the Ni K and the La L_3 edge support the theoretical calculations of Gupta for $LaNi_5$ and $LaNi_5H_7$. XANES results at the Ce L_3 edge indicate that hydriding causes Ce to convert from an α to a γ like state.

PUBLICATIONS

Mukerjee, S., McBreen, J., Reilly, J.J., Johnson, J.R., Adzic, G., Petrov, K., Kumar, M.P.S., Zhang, W., and Srinivasan, S. *In Situ* X-ray Absorption Studies of Metal Hydride Electrodes, Proceedings of Electrochemistry and Materials Science of Cathodic Hydrogen Absorption and Adsorption Symposium, 185th Meeting of the Electrochemical Society, San Francisco, CA, May 22-27, 1994, B. E. Conway and G. Jerkiewicz, Editors, The Electrochemical Society, Inc., Pennington, NJ (1995), pp. 104-119.

Adzic, G.D., Johnson, J.R., Reilly, J.J., Mukerjee, S., McBreen, J., Kumar, M.P.K., Zhang, W., and Srinivasan, S., Composition and Cycle Life and Multicomponent AB_5 Hydride Electrodes, Proceedings of Hydrogen and Metal Hydride Batteries Symposium, 186th Meeting of the Electrochemical Society, Miami Beach, FL, Oct. 9-14, 1994. P.D. Bennett, T. Sakai, Editors, The Electrochemical Society, Inc., Pennington, NJ (1994), pp. 24-32.

Mukerjee, S., McBreen, J., Reilly, J.J., Johnson, J.R., and Adzic, G., Effect of Ce Composition on the Structural and Electronic Characteristics of Some Metal Hydride Electrodes: An *In Situ* XANES and EXAFS Investigation, Proceedings of Hydrogen and Metal Hydride Batteries Symposium, 186th Meeting of the Electrochemical Society, Miami Beach, FL, Oct. 9-14, 1994. P.D. Bennett, T. Sakai, Editors, The Electrochemical Society, Inc., Pennington, NJ (1994), pp. 33-44 .

Mukerjee, S., McBreen, J., Reilly, J.J., Johnson, J.R., Adzic, G., Petrov, K., Kumar, M.P.S., Zhang, W., and Srinivasan, S., *In Situ* X-ray Absorption Spectroscopy Studies of Metal Hydride Electrodes, J. Electrochem. Soc., 142, 2278 (1995).

Adzic, G.D., Johnson, J.R., Reilly, J.J., Mukerjee, S., McBreen, J., Kumar, M.P.K., Zhang, W., and Srinivasan, S., Ceriun Content and Cycle Life and Multicomponent AB_5 Hydride Electrodes, J. Electrochem. Soc., 142, 3429 (1995).

Kumar, M. P. S., Zhang, W., Petrov, K., Srinivasan, S., Adzic, G. D., Johnson, J. R., Reilly, J. J., and Schwarz, R. B., Surface Modification, by Coating of Alloys, to Improve Performance of Metal Hydride Electrodes, Proceedings of Hydrogen and Metal Hydride Batteries Symposium, 186th Meeting of the Electrochemical Society, Miami Beach, FL, Oct. 9-14, 1994.

P.D. Bennett, T. Sakai, Editors, The Electrochemical Society, Inc., Pennington, NJ (1994), pp. 111-123.

Petrov, K., Visintin, A., Rostami, A. A., Anani, A., Srinivasan, S., Appleby, A. J., Reilly, J. J., Johnson, J. R., Lim, H. S. Investigation of AB_2 Alloys for Hydrogen Storage and Hydride Electrode, J. Electrochem. Soc. (submitted).

Kumar, M. P. S., Petrov, K., Zhang, W., Rostami, A. A., Srinivasan, S., Adzic, G. D., Johnson, J. R., Reilly, J. J., Lim, H. S., Effect of Ce, Co and Sn Substitution on Gas-phase and Electrochemical Hydriding/Dehydriding Properties of $LaNi_5$, J. Electrochem. Soc., 142, 3424 (1995).

INVITATIONS

J. McBreen, *In Situ* X-ray Spectroscopy Studies of Metal Hydride Electrodes, Gordon Research Conference on Hydrogen Metal Systems, Henniker, NH, July 16-21, 1995.

J. J. Reilly, Discussion Leader, "Hydrogen Behavior on Surfaces", ibid.

J. J. Reilly, "Properties of Metal Hydride Electrodes", presented at the Vice President's Automotive Technology Symposium #4, Washington D. C., September 1995.

SYNTHESIS AND CHARACTERIZATION OF METAL HYDRIDE ELECTRODES

1. CERIUM CONTENT AND CYCLE LIFE OF MULTICOMPONENT AB_5 HYDRIDE ELECTRODES

G. D. Adzic , J. R. Johnson, J. J. Reilly, J. McBreen, and S. Mukerjee, BNL;
M. P. Sridhar Kumar, W. Zhang and S. Srinivasan, Texas A&M University

Introduction

Multicomponent AB_5 hydrides are attractive as replacements for the cadmium electrode in nickel-cadmium batteries from both an environmental and performance viewpoint. However, the paradigm compound of the AB_5 class of alloys, $LaNi_5$, is not a suitable electrode because it corrodes rapidly in the chemically aggressive battery environment. This problem can be ameliorated by partial substitution of Ni by a variety of metals such as Co, Al, Si etc. The efficacy of this remedy has been attributed primarily to the reduction of the molar volume of hydrogen, V_H, in the hydride phase thereby reducing alloy expansion and contraction during the charge-discharge cycle. This in turn leads to a reduction of the flushing action of the electrolyte through the small pores and fissures of the alloy produced in the initial activation process. Consequently corrosion of the electrode is reduced (1). While the effects of Ni substitution have been widely studied, relatively little effort has focused on the effect of La substitution. This neglect is probably due to the good performance and low cost of mischmetal (Mm), which constitutes the A component in commercial AB_5 battery electrodes. The rare earth composition of mischmetal (Mm) corresponds to that of the ore body from which it is recovered; in bastnasite, the most common ore, it corresponds to (in atom%) 50-55 Ce, 18-28 La, 12-18 Nd, 4-6 Pr, <0.1 Sm, <2 others. The major component of mischmetal is Ce and this paper is focused on the determination of the effect of the substitution of Ce for La upon electrode cycle life and storage capacity. In pursuit of this goal we have examined the properties of a homologous series of alloys with a composition corresponding to $La_{1-x}Ce_xNi_{3.55}Co_{.75}Mn_{.4}Al_{.3}$ and measured their comparative performance as battery electrodes. Effects due to lattice expansion and hydride stability were addressed and accounted for. Henceforth, for the sake of brevity, alloys with this B_5 composition will be written as rare earths B_5, e.g., $La_{1-x}Ce_xB_5$. We will also compare their performance with MmB_5 electrodes.

Experimental

All the $La_{1-x}Ce_xB_5$ alloys were prepared from high purity, >99.9%, starting components. Mischmetal alloys were prepared using commercial mischmetal. In one case a synthetic mischmetal alloy was prepared using high purity La, Ce, Nd and Pr. A baseline $LaNi_{4.7}Al_{.3}$ electrode was also prepared using a commercial alloy obtained from the Ergenics Corporation, Ringwood, NJ. Except for $LaNi_{4.7}Al_{.3}$ all the alloys were prepared by arc melting under helium. After the first melt the ingot was inverted and re-melted twice. Each ingot was annealed at 1173K for 3 days after which X-ray diffraction patterns were obtained for each alloy and its lattice parameters determined. Pressure-composition (P-C) isotherms were measured for all alloy

compositions according to the usual procedure (2). The molar volume of hydrogen in the hydride phase was determined by preparing the hydride phase via the gas-solid reaction under a H_2 pressure of 10 atm. The reactor was then cooled to 78K and evacuated. CO was introduced into the reactor and allowed to condense, after which it was slowly warmed to room temperature, venting CO as necessary to avoid excess pressurization. At 298K the system was vented and the sample removed. This procedure effectively poisoned the alloy surface and prevented hydride decomposition in air for at least several days and permitted X-ray diffraction patterns of the hydride phase to be obtained in sample holders open to the atmosphere (3). After poisoning the alloy hydride was split into three portions; one used in the X-ray procedure and the other two were subjected to hydrogen analyses via thermal decomposition.

Electrodes were fabricated from a portion of each alloy and subjected to electrochemical cycling studies. Each electrode was prepared by mixing -100 mesh alloy particles with a mixture of Teflon suspension and carbon black(Vulcan XC-72) in the weight ratio of 17% teflon, 33% carbon black and 50 % alloy (4). The weight of the AB_5 intermetallic alloy was 0.075 g. The mixture was then mechanically pressed onto a nickel mesh screen attached to a Ni wire connection which was then sandwiched between two nickel foam (Eltech Corp., Fairport Harbor Ohio) disks 1.7 cm^2 in diameter. Finally two Al foil disks were pressed lightly onto each side of the electrode after which the assembled electrode was inserted into a hydraulic press and pressed at 12000 psi. The apparent electrode surface area was 4.5 cm^2. After pressing the Al foil was removed by dissolving it in concentrated KOH. The electrode was then introduced into an electrochemical cell containing 6 M KOH electrolyte and open to the atmosphere. The counter electrode was a Pt grid and the reference electrode was Hg/HgO. The electrode was activated in situ via successive electrochemical charge and discharge cycles. The cycle life measurements were carried out using a computer controlled battery cycler (Arbin Corp., College Station Texas). After activation the charging rate was kept constant at 15 mA for two hours, which is approximately equivalent to a rate of 0.66C. The discharge current was constant at 10 mA (0.5C rate); it was cutoff when the anodic voltage decreased to -0.70 V vs. the Hg/HgO reference electrode.

Results and Discussion

I: X-ray Diffraction

The variation of the volume of the AB_5 unit cell as a function of x in $La_{1-x}Ce_xB_5$ is shown in Figure 1. The cell volume is of interest because it can be correlated with the stability of the hydride phase in any homologous alloy series (5). The cell volume is also a linear function of the Ce content and is a useful check on the intermetallic composition. The equation for the cell volume as a function of x is;

$$Cell\ volume = (-4.5058x + 89.300)\text{Å}^3 \qquad (1)$$

The lattice parameters of the starting alloys, their respective hydride phases and the molar volume of hydrogen, V_H, in the latter are listed in Table 1. All of the samples could be indexed as having hexagonal symmetry and were essentially single phase. For the

calculation of V_H, the unit cell is assumed to contain one formula unit for both the metal and the hydride phases. V_H is based on the expansion of the hexagonal unit cell per H atom inserted, n, i.e.,

$$V_H = (Vol_{AB5Hn} - Vol_{AB5})(n^{-1}) \quad (2)$$

where the units of volume are $Å^3$.

Attention should be called to the low V_H in CeB_5H_n. The lower value of V_H in the H solid solution region (α phase) is not without precedent, e.g. in $LaNi_5H_{0.165}$ V_H is reported to be 2.6 $Å^3$ per H-atom whereas in the hydride phase (1) it is 3.5 $Å^3$ (6).

II: Pressure Composition Isotherms

Pressure-composition (PC) isotherms for $La_{1-x}Ce_xB_5$ alloys are shown in Figure 2. There is very little hysteresis in the more stable systems ($x < 0.75$) and only absorption isotherms are shown for the sake of clarity.

The maximum H content for $La_{1-x}Ce_xB_5$ is achieved when $x = 0.2$; however at $x > 0.2$ there is a decrease in the H storage capacity and hydride stability until at $x = 1$ the decrease in both stability and storage capacity is marked. This trend is not unexpected as the unit cell volume decreases with Ce content (Fig. 1). It is also quite obvious that the B_5 composition greatly influences hydride stability since the desorption plateau pressure for $CeNi_5H_x$ is reported to be 90 atm at 295K (7).

In Figure 3 we show both absorption and desorption PC isotherms for MmB_5H_x and $LaNi_5H_x$. Only the latter exhibits a significant hysteresis effect. It may be mentioned that the lack of hysteresis near room temperature in multicomponent AB_5 hydrides is not unusual, but it is almost always present in the less complex binary and ternary systems. It is noteworthy that, with one exception ($x = 0.2$ in $La_{1-x}Ce_xB_5$), all the multicomponent alloys have significantly less hydrogen storage capacity then $LaNi_5H_x$. This is the usual consequence of the substitution of Ni and La by other metals.

III: Cycle Life

The cycle life of $La_{1-x}Ce_xB_5$ and MmB_5 electrodes are illustrated graphically in Figures 4 and 5 by plotting the electrochemical discharge capacity, Q, vs. cycles. Inspection of the individual plots reveals the following general behavior. There is an initial steep increase in capacity in the first few cycles; this comprises the activation process which consists of particle size reduction and surface reconstruction. After activation a maximum in electrochemical storage capacity, Q_{max} ,is reached. This is usually followed by an essentially linear decrease in capacity as a function of cycles which may be termed capacity decay. It is defined as the slope of the capacity vs. cycle curve, i.e., -dQ/dcycle, and determined via a least squares fit of the data as shown in Figure 5.

The decreased capacity found in all $La_{1-x}Ce_xB_5$ alloys (Fig. 4) with $x > 0.35$ conforms to the shorter and higher plateau pressures of the isotherms depicted in Figure 2. The extremely low electrochemical capacity of CeB_5 is obviously a consequence of the high instability of the hydride phase. Most cycle experiments were repeated but only one plot for each composition is shown in Figure 4. However all the experiments and results are listed in Table 2. In order to confirm the behavior of LaB_5 three cycle life experiments were carried out using two separate alloys (electrodes T54, 30, 51). The value for V_H as shown in Table 2 for LaB_5 is the average of the two determinations shown in Table 1. In all three experiments capacity decay (-dQ/dcycle) was very reproducible and relatively high.

The cycle life data in Table 2 are listed in order of increasing capacity decay. Two electrodes $La_{.25}Ce_{.75}B_5$ and MmB_5 (No.'s 29 and 24), have been subjected to 300 or more cycles without any significant loss in storage capacity. This is good evidence that the physical integrity of all the electrodes, prepared as described in the Experimental Section, is very good and that the decay and corrosion rates listed in Table 2 and calculated from the plots in Figure 4 and 5 are due to electrode corrosion and not experimental artifacts.

In order to determine the effect of Ce substitution it is necessary to quantitatively determine lattice expansion. Thus Table 2 lists a new parameter, $\Delta\epsilon$, in addition to the H content, n, and capacity decay. $\Delta\epsilon$ is a function of V_H and the H content, here expressed as the number of H atoms, n, per formula unit. n is calculated from Q_{max} via the Faraday equation,

$$n = e^- = 3600(mw \times Q_{max})(9.65 \times 10^7)^{-1} \qquad (3)$$

where *mw* is the molecular weight of the alloy and the units of Q are mAh/g. It is assumed that after activation the remaining uncorroded alloy in each subsequent charge-discharge cycle is hydrided and dehydrided to the same degree and n is constant. Note however that Q is usually not constant since it is a function of the weight of the uncorroded alloy in each cycle. Thus for the unit cell, which contains one formula unit, undergoing the phase conversion process,

$$\Delta\epsilon = V_H \times n \qquad (4)$$

where is the actual volume change of the unit cell in $Å^3$ in each charge or discharge cycle.

In the series $La_{1-x}Ce_xB_5$ the greatest values of $\Delta\epsilon$ correspond to compositions where x = 0.2 and 0.35 (electrodes 47,T50, 26) yet the capacity decay for these alloys is significantly less than that for the unsubstituted alloys (electrodes 30, 51, T54). It is not at all surprising that the decay rate is very low for x = .75 (No. 29) because it absorbs significantly less hydrogen than the samples with reduced Ce content and, therefore, $\Delta\epsilon$ is low.

The normal MmB_5 electrodes (No.'s 24, 21-2,) have a very low decay rate, but they also have a lower capacity and low $\Delta\epsilon$. The synthetic MmB_5 electrodes (No.'s 27,46) have a higher storage capacity than the normal Mm electrodes and, since V_H is about the same, a higher $\Delta\epsilon$ and decay rate. However, at present it is not possible to discriminate between $\Delta\epsilon$

or the composition of the A component as the cause of the higher decay rate of the synthetic Mm alloy.

The behavior of the CeB_5 electrode (No. 36) is instructive. It has very low capacity because of the instability of the hydride phase as shown in Figure 2. The low decay rate is due to low storage capacity and a very low $\Delta\epsilon$. Thus the rate of fracturing of the intermetallic is greatly reduced because $\Delta\epsilon$ is very small. Consequently the rate of surface area increase per cycle is diminished and the activation process is retarded. As shown in Figure 4, Q_{max} for this electrode is not reached until it was subjected to 100 cycles. Unfortunately it was not possible to measure V_H in the hydride phase because it was too unstable and lost H_2 when it was subjected to X-ray diffraction.

The $LaNi_{4.7}Al_3$ electrode (no. 11) was used as a baseline comparison with the more complicated alloy electrodes discussed herein. This relatively simple intermetallic forms a hydride phase somewhat more stable than $LaNi_5$ with a slightly reduced H content (8). Even though $\Delta\epsilon$ is less than several of the other more complex electrodes, the decay rate is the highest measured. This again illustrates the point that $\Delta\epsilon$ is not the sole criterion of electrode corrosion but rather that composition also plays a very important role; in this case the deciding factor is the B_5 composition (compare $LaNi_{4.7}Al_3$ and LaB_5 electrodes). We have also included in Table 2 a calculated $\Delta\epsilon$ of 21 $Å^3$/unit cell for $LaNi_5$ from data abstracted from Willems and Buschow (1); it exceeds that for any other alloy by a large margin. Consequently it is not surprising that an $LaNi_5H_x$ electrode is reported to have a very high decay rate (1).

IV: Alloy Corrosion

The corrosion of AB_5 electrodes has been proposed to occur via the irreversible oxidation of the alloy to form rare earth hydroxides. In the case of a cycled $LaNi_5$ electrode it was determined by transmission electron spectroscopy that $La(OH)_3$ was present after cycling (1). In the present instance an $La_{.8}Ce_{.2}B_5$ electrode subjected to 700 charge discharge cycles was found to contain $La(OH)_3$, $Ce(OH)_3$ and Ni metal as determined by x-ray diffraction. The presence of rare earth hydroxides, Ni and nickel oxides have been reported in electrochemically cycled AB_5 electrodes as determined by X-ray near edge spectra (XANES) (9) and X-ray photoelectron spectroscopy (XPS) studies (10). Thus the loss of electrochemical capacity is directly proportional to the loss of the AB_5 alloy by oxidation and readily calculated as follows;

$$\frac{d[AB_5]}{dcycle} = \left[\frac{-dQ}{dcycle}\right](Q_{max})^{-1} \times 100 \qquad (5)$$

where the units of AB_5 are mol %. This equation is valid provided that the physical integrity of the electrode is maintained. The corrosion rate for all alloys, in units of mol%/cycle, is given in Table 2. The effect of Ce content upon electrode corrosion is clearly shown in Figure 6 which illustrates plots of alloy corrosion and $\Delta\epsilon$ versus Ce content for all the $La_{1-x}Ce_xB_5$ electrodes (data for electrode T47 is included despite the slightly reduced Ni

content). There is a precipitous decrease in alloy corrosion rate between x = 0 and 0.2 despite the fact that $\Delta\epsilon$ actually increases slightly. On the basis of lattice volume change one would predict a slight increase in corrosion. Upon further increase in Ce content the corrosion rate again can be correlated to $\Delta\epsilon$. The results are clear and unequivocal; the presence of a relatively small amount of Ce can greatly reduce corrosion even though $\Delta\epsilon$ may be unchanged or even increased.

Summary and Conclusion

From the above considerations we have concluded that corrosion and the consequent decay in storage capacity of $La_{1-x}Ce_xB_5$ electrodes is not solely a function of the volume change per cycle, , but also rare earth composition. The presence of a small amount of cerium has been shown to retard corrosion irrespective of lattice expansion/contraction due to hydride formation/decomposition. A possible explanation for this finding lies in the fact that Ce can form a protective oxide film on metal surfaces (Al, mild steel and others) and it has been shown via XANES (X-ray Absorption Near Edge Structure) studies that Ce in the film is present as four valent CeO_2 (11). Recent work has reported that Ce in the unhydrided bulk alloy of $La_{.8}Ce_{.2}Ni_{4.8}Sn_{.2}$ is present as a four valent atom. Further we note that although the MmB_5 electrode has only a modest storage capacity such electrodes are useful because of their extended lifetime (possibly due to the formation of a protective coating of CeO_2 on the alloy surface). However, a battery incorporating a $La_{1-x}Ce_xB_5$ electrode with x = 0.2 would have a better overall performance than one with a normal MmB_5 electrode although it would be more costly. A more practical alternative may be to use mischmetal with reduced Ce content, e.g. ~20 atom%, for battery electrodes; this would tend to increase storage capacity without sacrificing corrosion resistance. In this connection it is of interest to point out that two other major components of mischmetal, Pr and Nd, may also form four valent oxides and both have been reported to form protective oxide films (12). Finally, if the reduced corrosion attributed to the presence of Ce is indeed due to a mechanism involving the surface formation of CeO_2 then its inclusion in other types of metal hydride electrodes may have a similar beneficial effect.

References

(1) J. J. G. Willems and K. H. J. Buschow, J. Less-Common Metals, 129, 13 (1987).

(2) J. J. Reilly and R. H. Wiswall, Inorganic Chem., 13, 218(1974).

(3) J R. Johnson and J. J. Reilly, Inorganic Chem., 17, 3103(1978).

(4) K. Petrov, A. A. Rostami, A. Visintin and S. Srinivasan, J. Electrochem. Soc., 141, No.7, 1747(1994).

(5) D. N. Gruen, M. H. Mendelsohn and A. E. Dwight, J. Less Common Metals, 56, 19 (1977).

(6) J. F. Lynch and J. J. Reilly, J. Less-Common Metals, 87, 225 (1982).

(7) S. N. Klyamkin and V. N. Verbetsky, J. of Alloys and Compounds, 194, 41 (1992).

(8) M. Mendelsohn, D. M. Gruen and A. E. Dwight, J. Less-Common Metals, 63, 193 (1979).

(9) S. Mukerjee, J. McBreen, J. J. Reilly, J. R. Johnson and G. Adzic, Proceedings of Hydrogen and Metal Hydride Batteries Symposium, 186th Meeting of the Electrochemical Society, Miami Beach, FL, Oct. 9-14, 1994. P.D. Bennett, T. Sakai, Editors. The Electrochemical Society, Inc., Pennington, NJ (1994), pp. 33-44 .

(10) F. Meli, A. Zuettel and L. Schlapbach, J. of Alloys and Compounds, 190, 17-24 (1992).

(11) A. J. Davenport, H. S. Isaacs and M. W. Kendig, Corrosion Science, 32, No. 5/6, 653 (1991).

(12) D. R. Arnott, B. R. W. Hinton and N. E. Ryan, Corrosion, 45, 12(1989).

TABLE 1
LATTICE PARAMETERS AND V_H

COMPOSITION	ALLOY #	a A	c A	CELL VOL A^3	V_H A^3/atom
LaB_5	2040	5.0642	4.0325	89.56	
$LaB_5H_{5.84}$	2040	5.3911	4.2387	106.69	2.93
LaB_5	2059	5.0615	4.0298	89.40	
$LaB_5H_{6.01}$	2059	5.3985	4.2728	107.77	3.05
$La_{.8}Ce_{.2}B_5$	2036	5.038	4.0416	88.84	
$La_{.8}Ce_{.2}B_5H_{5.91}$	2036	5.3985	4.2728	107.84	3.21
$La_{.65}Ce_{.35}B_5$	2058	5.0168	4.0451	88.16	
$La_{.65}Ce_{.35}B_5H_{5.68}H$	2058	5.3790	4.2522	106.54	3.24
$La_{.5}Ce_{.5}B_5$	2034	4.9934	4.0446	87.33	
$La_{.5}Ce_{.5}B_5H_{5.55}$	2034	5.353	4.2229	104.79	3.15
$La_{.25}Ce_{.75}B_5$	2033	4.9538	4.0559	86.19	
$La_{.25}Ce_{.75}B_5H_{2.84}$	2033	5.1546	4.1358	95.16	3.15
CeB_5	2061	4.9226	4.0523	85.04	
$CeB_5H_{0.62}$ (α phase)	2061	4.9365	4.0766	86.03	1.60
MmB_5 (Synthetic Mm)	2049	4.9890	4.0545	87.39	
$MmB_5H_{4.60}$ (Synthetic Mm)	2049	5.2945	4.1872	101.65	3.10
MmB_5	2063	4.9626	4.0560	86.50	
$MmB_5H_{3.12}$	2063	5.1853	4.1335	96.25	3.13
$MmNi_{3.5}Mn_{.4}Al_{.3}Co_{.75}$	2031	4.9623	4.0456	86.27	
$MmNi_{3.5}Mn_{.4}Al_{.3}Co_{.75}H_{3.34}$	2031	5.209	4.1309	97.07	3.23
$LaNi_{3.5}Mn_{.4}Al_{.3}Co_{.75}$	2032	5.0699	4.0392	89.91	
$LaNi_{3.5}Mn_{.4}Al_{.3}Co_{.75}H_{6.11}$	2032	5.4074	4.2743	108.23	3.00
$LaNi_{4.7}Al_{.3}$		5.0195	4.0076	87.44	
$LaNi_{4.7}Al_{.3}H_{5.30}$		5.3385	4.2558	105.82	3.47

TABLE 2
CYCLE LIFE OF MODIFIED AB_5 ELECTRODES
$B_5 = Ni_{3.55}Co_{.75}Mn_{.4}Al_{.3}$

ELECTRODE	MW	ELECT. #	V_H, A^3/atom	n H atoms unit cell	$\Delta\varepsilon$ A^3/unit cell	CYCLES	Q_{max} mAh/g	DECAY -dQ/dcy mAh/g·c	ALLOY CORR. mol%/c
CeB_5	422	36	1.60	0.8	1.3	180	51	0.0	0.0
MmB_5	422	24	3.13	3.9	12.2	400	247	0.004	0.002
$La_{.25}Ce_{.75}B_5$	422	29	3.15	3.8	12.0	300	241	0.015	0.003
$MmNi_{3.50}Mn_{.4}Al_{.3}Co_{.75}$	420	21-2	3.23	3.6	11.6	140	230	0.041	0.018
$La_{.5}Ce_{.5}B_5$	422	T49	3.15	4.4	13.9	230	278	0.11	0.040
$La_{.8}Ce_{.2}B_5$	421	58	3.21	4.8	15.4	130	305	0.13	0.042
$La_{.8}Ce_{.2}B_5$	421	6	3.21	4.6	14.7	92	293	0.14	0.047
$La_{.5}Ce_{.5}B_5$	422	32	3.15	4	12.8	275	260	0.14	0.054
$La_{.8}Ce_{.2}B_5$	421	37	3.21	4.6	14.8	190	293	0.15	0.051
$La_{.8}Ce_{.2}B_5$	421	T50	3.21	5.0	16.1	80	318	0.18	0.057
$La_{.65}Ce_{.35}B_5$	422	26	3.24	5.0	16.2	303	318	0.18	0.057
MmB_5 (synthetic)	423	46	3.10	4.4	13.7	130	279	0.19	0.068
$La_{.8}Ce_{.2}B_5$	422	47	3.21	5.0	16.1	150	318	0.21	0.066
MmB_5 (synthetic)	423	27	3.10	4.3	13.3	200	273	0.26	0.095
$LaNi_{3.50}Mn_{.4}Al_{.3}Co_{.75}$	420	T47	3.23	4.9	14.7	140	313	0.41	0.130
LaB_5	421	T54	2.99	4.8	14.3	75	305	0.46	0.150
LaB5	421	51	2.99	5.2	15.5	150	331	0.46	0.139
LaB_5	421	30	2.99	5.1	15.2	125	325	0.47	0.145
$LaNi_{4.7}Al_{.3}$	423	11	3.47	4.5	15.6	125	285	0.83	0.291
$LaNi_5$ (Ref. 1)		-	3.5	6.0	21.0	-	372	45%loss 100cycle	

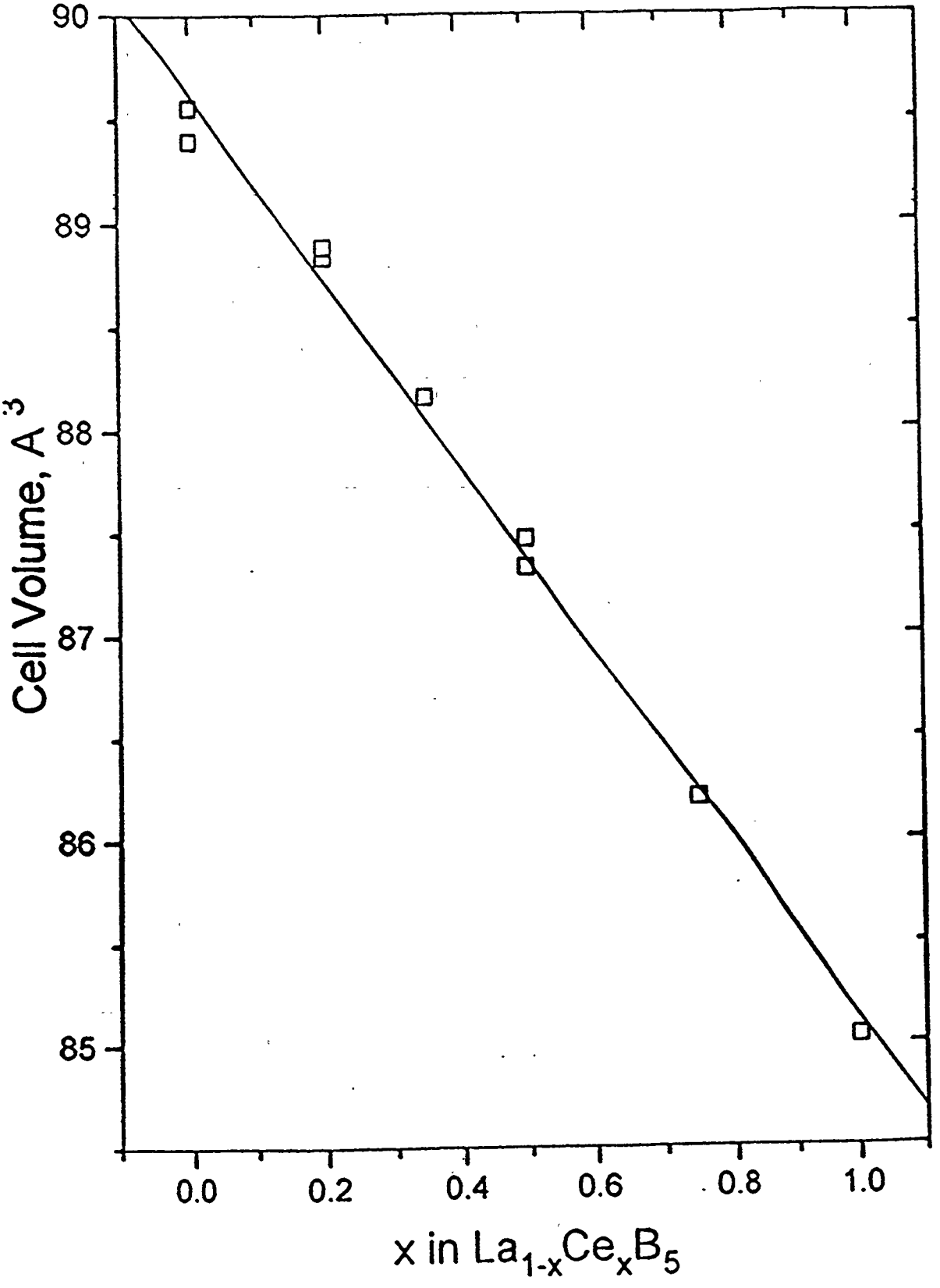

Figure 1: Variation of the unit cell volume of $La_{1-x}Ce_xB_5$ with x.

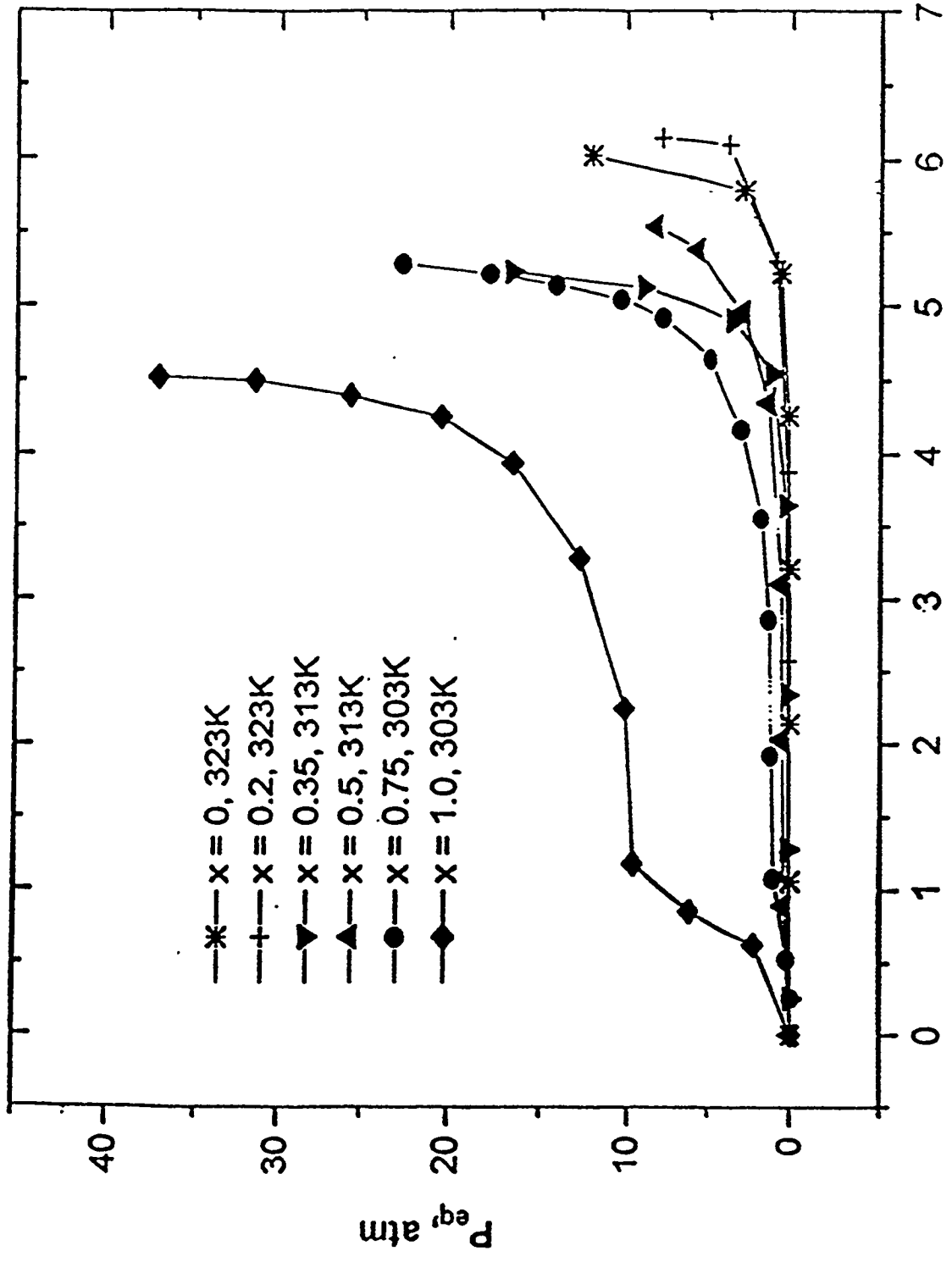

Figure 2: Pressure Composition isotherms of the $La_{1-x}Ce_xB_5$ system; ✳, x = 0 (323K); +, x = 0.2 (323K); ▼, x = 0.35 (313K); ▲, x = 0.5 (313K); ●, x = 0.75 (303K); ◆, x = 1 (303K).

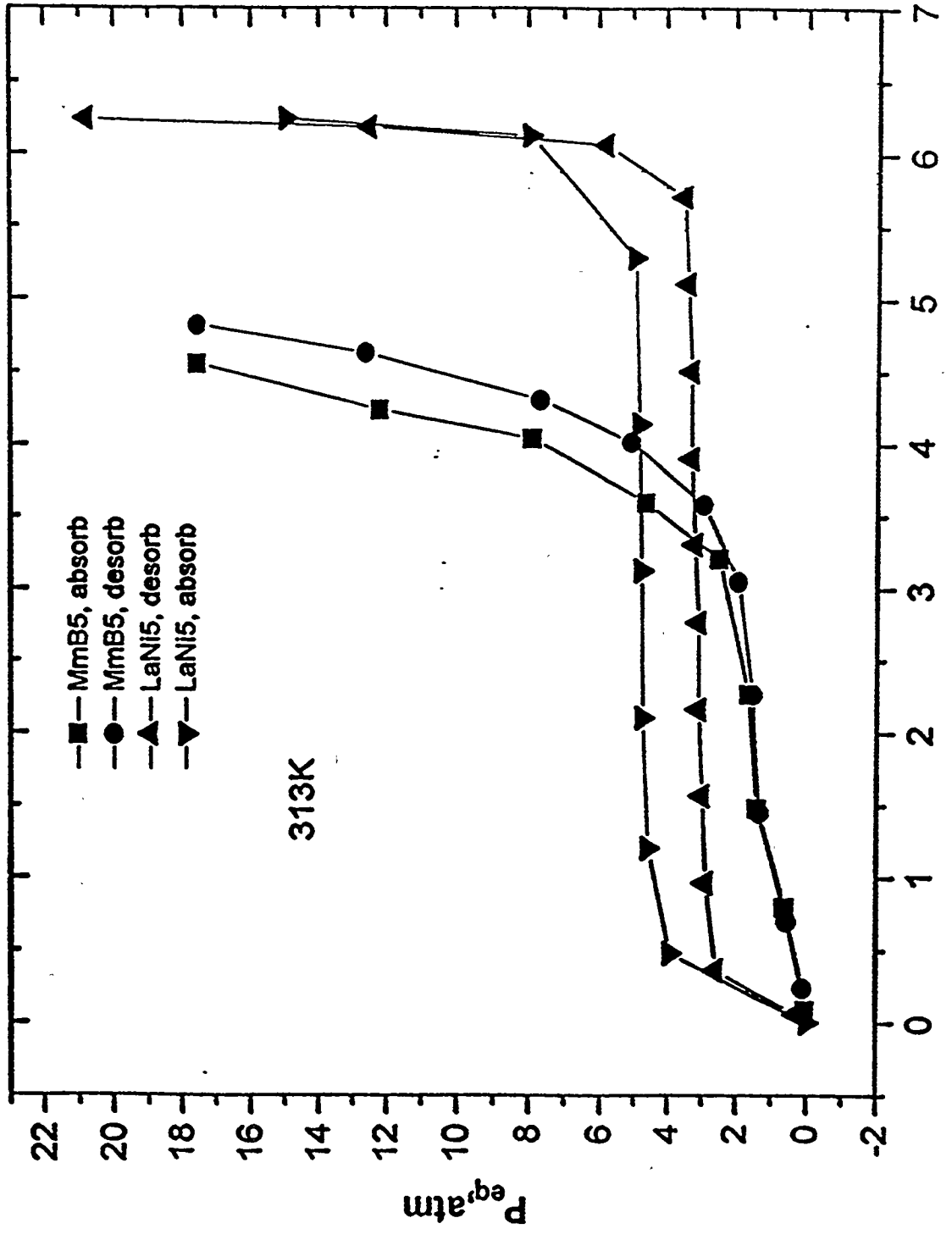

Figure 3: Pressure composition isotherms for $LaNi_5$, and MmB_5; ▲, desorption $LaNi_5$; ▼, absorption $LaNi_5$; ●, desorption MmB_5; ■, absorption MmB_5.

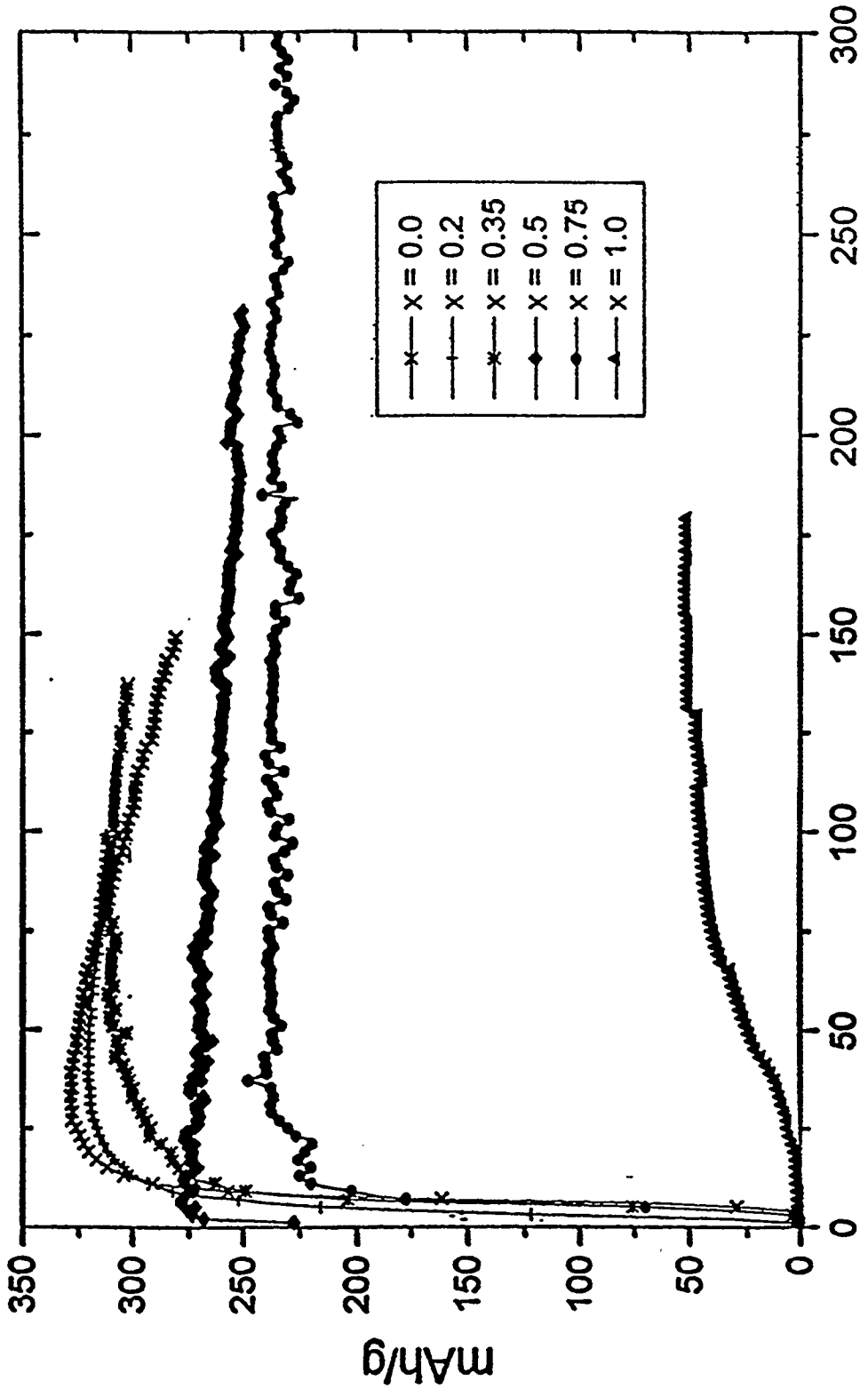

Figure 4: Capacity , Q, versus charge - discharge cycles for $La_{1-x}Ce_xB_5$ electrodes; X, x = 0.0; +, x= 0.2; *, x = 0.35; ◆, x = 0.5; ●, x= 0.75; ▲, x = 1.0. Only every third data point is shown.

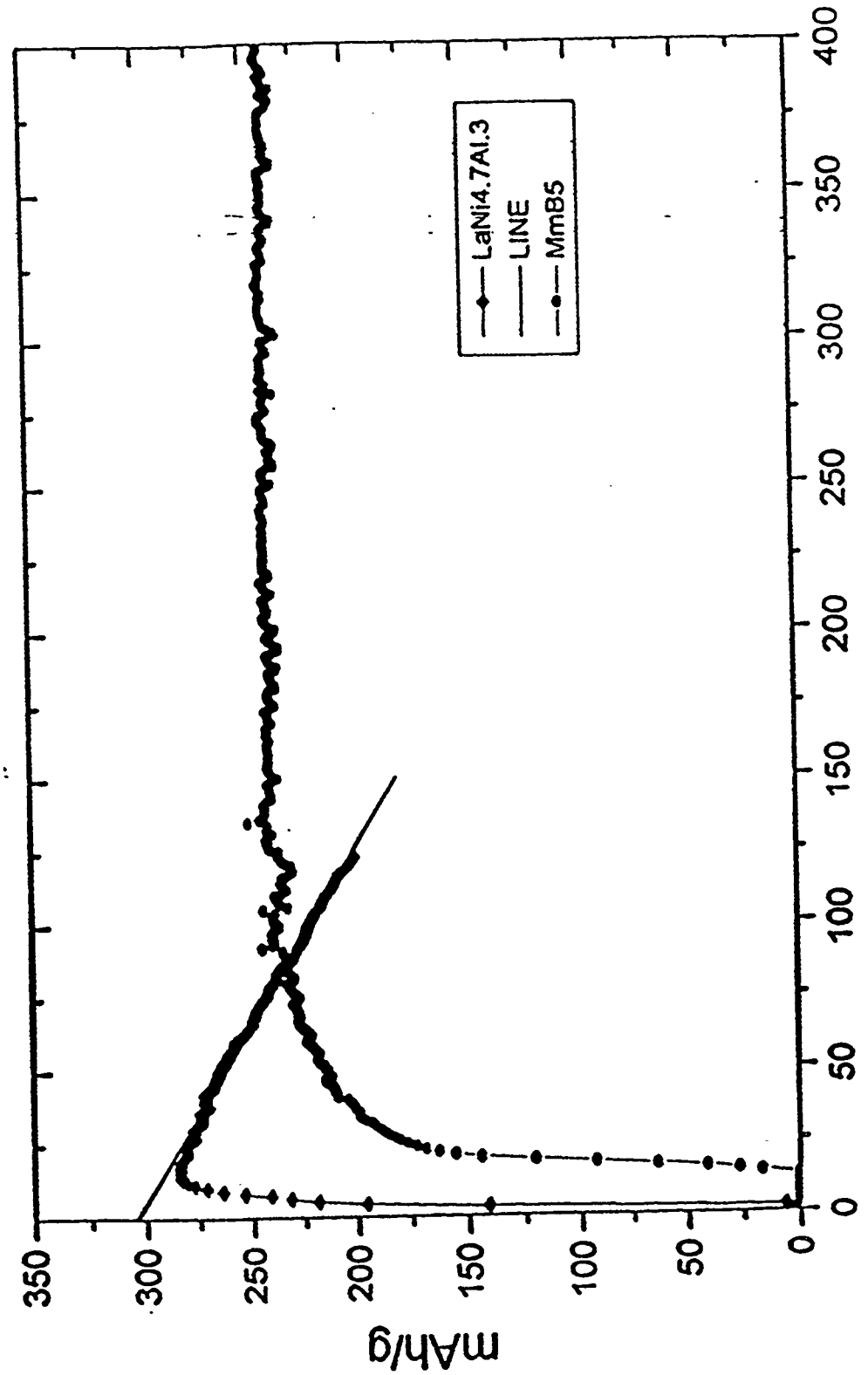

Figure 5: Capacity , Q, versus charge - discharge cycles for two electrodes, ●, MmB_5 and ◆, $LaNi_{4.7}Al_{.3}$. A linear least squares line is shown for the latter plot.

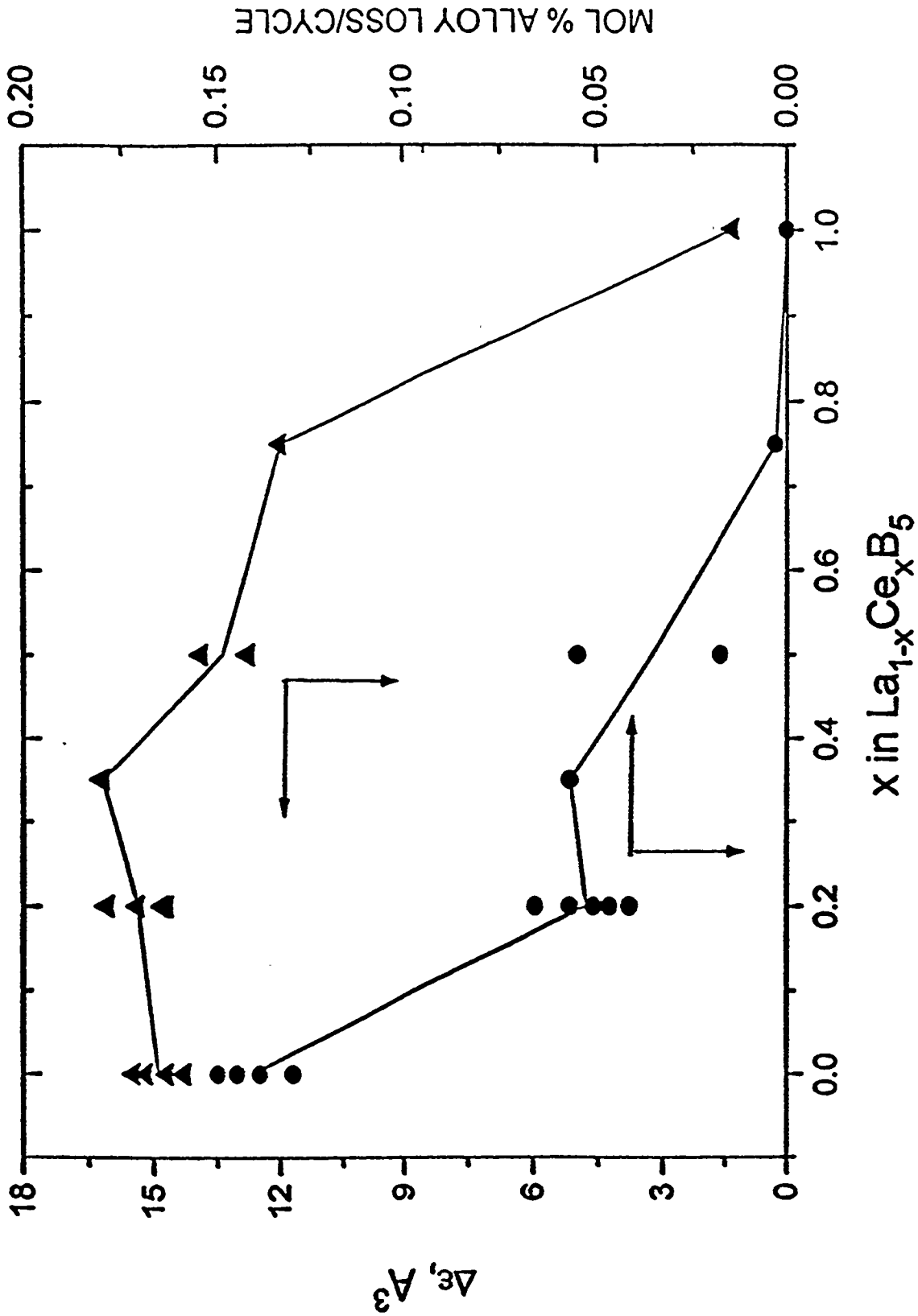

Figure 6: ▲, Δε and ●, alloy corrosion (mol%/cycle); the solid line is drawn through the average Y value when more than one Y value is given.

2. *IN SITU* XAS STUDIES OF METAL HYDRIDE ELECTRODES

S. Mukerjee, J. McBreen, J. J. Reilly, J. R. Johnson and G. Adzic, BNL
K. Petrov, M. P. S. Kumar, W. Zhang and S. Srinivasan,Texas A&M University

Introduction

Recent advances in the development of stable metal hydride alloy electrodes has led to their use as a replacement for cadmium anodes in rechargeable alkaline batteries (1). Present battery electrodes are either AB_2 or AB_5 type alloys. The performance and life of these alloys greatly depend on their composition. In the case the AB_5 type alloys, substitution of either component in the prototype alloy, $LaNi_5$, with small amounts of other alloying elements can have major effects in the performance and stability of the alloy. Previous results with Ce, Sn and Co substitution have demonstrated promising results in battery electrodes (2). Recent results (3) have shown that Sn and Co substitution for some of the Ni causes a lowering of the hydrogen plateau pressure. Partial substitution of La with Ce results in improved corrosion resistance and cycle life. The Ce substitution also causes an increase in the hydrogen plateau pressure. An understanding of the mechanism of these effects would help in optimizing metal hydrides for various hydrogen storage and battery applications.

Most previous studies to understand the role of various substituents in metal hydride alloys have focused on the structural aspects of such substitutions (via application of X-ray and neutron diffraction techniques). However, electronic effects, such as the role of empty *d* states are important for hydrogen storage (4).

X-ray absorption spectroscopy (XAS) has the ability to probe *in-situ,* both electronic (from the X-ray absorption near edge structure, XANES) and geometric parameters (from the extended X-ray absorption fine structure, EXAFS) with element specificity. Most previous XAS studies on hydrides have been done in the gas phase. Tanaka *et al* (5) and Lengeler and Zeller (6) did early XANES work on several metal hydrides. In the case of $NiH_{0.85}$, changes in the XANES on hydriding were attributed to changes in the density of empty *p* states (6). Similar conclusions were made for $VH_{0.73}$ (5). Later Garcia *et al.* used both XANES and EXAFS to study the alloy hydrides $CeRu_2H_{3.75}$ and $CeFe_2H_{3.75}$ at the Ce L_3 edge and the Fe K edge (7). More recently Suenobu *et al.* have done XAS studies on amorphous $LaNi_5$ thin films, involving gas phase hydriding (8, 9). Recently, an *in-situ* XAS study on $LaNi_5$ electrode has been reported (10).

The present study focuses on the application of *in-situ* XAS to elucidate the electronic and geometric parameters as a result of (a) substitution of both A and B components of the prototype AB_5 alloy, $LaNi_5$, by Ce and Sn and (b) the effect of charging and discharging the metal hydride electrode in 6 M KOH.

Experimental

Alloy Preparation and Characterization: All the alloys were prepared from high purity (> 99.9 %) starting components with the exception of Ce, which was of commercial purity. The alloys were prepared by an arc melting technique under He atmosphere. The melting procedure involved several remelting steps, each time followed by turning over the ingot. This was followed by an annealing step at a temperature of 1173K for 48 hours, after which X-ray diffraction patterns were obtained for each alloy and its lattice parameters determined.

The alloys were first characterized by obtaining the hydrogen pressure composition isotherms (PCT) in a modified Sievert's type apparatus according to the usual procedure (11). This yielded the hydrogen plateau pressure and the hydrogen equilibrium storage capacity in the gas phase. The molar volume of hydrogen in the hydride phase was determined by comparing the lattice parameters of the hydrided and dehydrided phases using X-ray diffraction. The procedure for determining the lattice parameter and molar volume of hydrogen is given elsewhere (12).

Electrochemical and Cycling Studies: Electrochemical characterization measurements and cycling tests were made on electrodes prepared by pressing a mix, comprising of the alloy, carbon black (Vulcan XC-72) and 33 wt% PTFE binder (Teflon T-30), on to a 80 mesh nickel screen. The electrodes were tested for their initial capacity, charge-discharge characteristics and cycle life in 6 M KOH. The electrode potential was monitored using Hg/HgO reference electrode and the capacities were measured to a cut of potential of -0.7 V. Cycle life was measured using a Bitrode battery cycler by charging at 0.5C rate for 3 hours and discharging at the same rate to a cut off cell potential of 1.0V versus a nickel hydroxide counter electrode. After cycling, the electrodes were washed to remove KOH. The active material was removed from the current collector, mixed with boron nitride (BN) and pressed into a pellet for XAS studies.

In-situ XAS Studies: X-ray absorption spectroscopic (XAS) measurements were conducted at the Beam Lines X23A2 and X11 at the National Synchrotron Light Source (NSLS). Details of the monochromator design and energy resolution of the respective Beam Lines are given in detail elsewhere (13-15). To eliminate second harmonics the beam was detuned by 15 % at the Ni K edge and by 50 % at the La and Ce L edges. *In-situ* XAS measurements were made, in the transmission mode, at the La L_3, Ni K and Ce L_3 edges, at the end of charge and discharge. The electrodes for the *in-situ* XAS measurements and for measurements on dry samples were thin discs (0.25 mm thick and 19 mm in diameter) that comprised of the alloy, carbon black (Vulcan XC-72), vitreous carbon fibers and a polyvinylidine fluoride binder. They were prepared using a standard vacuum table paper making technique (13). Prior to electrode fabrication, all the alloys were activated by subjecting each to several hydriding-dehydriding cycles in the Sievert' s apparatus. This produces a fine powder with a BET surface area of ~ 0.5 m^2/gm, or a particle size of ~5μm that eliminates thickness effects in the EXAFS and avoids the need for an electrochemical activation procedure. In the last dehydriding cycle the H content of the solids was measured by venting aliquots of desorbed H_2 gas into a measured volume; these values are listed in Table 1. For detailed accounts of the activation procedure see refs., 16-17. The

separator was a single layer of a polyamide felt (0.125 mm thick) combined with a single layer of a 0.025 mm thick radiation grafted polyethylene separator. The counter electrode was a 0.125 mm thick Grafoil disc. All components were soaked in 6 M KOH and incorporated into a spectro-electrochemical cell that is described elsewhere (13). The data acquisition for XAS comprised of three 12 inch ionization detectors (incidence I_o, transmittance I_t, Reference I_{ref}). The reference channel was primarily for internal calibration of the edge positions and was used in conjunction with pure foils or oxide samples of the respective elements. For the Ni K edge pure N_2 was used in all the chambers, while for the La/Ce L_3 edges a mixture of 80%He and 20%N_2 was used in the incidence chamber while passing pure N_2 in the transmittance and reference chambers.

The metal hydride electrodes for the *in-situ* studies were charged at a constant current of 1 mA for 16h and discharged at a current of 2 mA to a potential of -0.5 V. The charging rate and time, allowed for considerable overcharge because the electrodes contained only ≈50 mg of the alloy. XAS scans were run within 30 minutes of the termination of charge.

Data Analysis: The data analysis package used for the XANES analysis was the University of Washington analysis program (18). The data analysis was done according to procedures described in detail elsewhere (13-15,18-21). The EXAFS data analysis used computer algorithms developed by Koningsberger and coworkers (18-21). The most comprehensive analysis of EXAFS was carried out on the data for dry uncycled electrodes at the Ni K edge. The Fourier filtering and analysis of the EXAFS spectra were conducted according to procedure described in detail elsewhere (13-15, 22). The windows for the forward and inverse Fourier transforms were chosen on the basis of nodes in the EXAFS in order to avoid excessive termination errors (23). The slight variations in the Δk and Δr ranges however do not effect the outcome of the results (23). The analysis was confined to the first major peak in the Fourier transform at 2.2 Å. Analysis of the EXAFS spectra for the alloys was done using one, two, three and four shell fits using an iterative least square technique (24). For fitting the sample data, phase and amplitude parameters derived from standard materials as well as those calculated using the University of Washington FEFF program (version 4.08) were employed (25). The phase and amplitude parameters for Ni-Ni coordination shells were obtained from liquid N_2 data for a pure Ni foil (6 μm thick). The Ni-La and Ni-Sn phase and amplitude parameters were calculated theoretically using the FEFF program based on Cartesian coordinates input for the Wurtzite structure. The cell constants were varied to yield first shell bond distances that were equivalent to the sum of the atomic radii. In these theoretical calculations an S_o^2 value of 0.7 was used throughout.

Results and Discussion

X-ray Diffraction, Physico-chemical and Electrochemical Characterization: Table 1 shows the results of X-ray diffraction analysis for the alloys. All the alloys were single phase and possessed the hexagonal $CaCu_5$ type (space group P6/mmm) structure, typical of the AB_5 type alloys. As indicated by the lattice parameters in Table 1, substitution of B component (Ni) by Sn in the AB_5 metal hydride lattice ($LaNi_5$) results in an increase in the lattice parameters and hence the cell volume. However, substitution of the A component (La) with Ce causes a minor shrinkage along

the *a* axis. The structural change due to partial substitution of Ni by Sn is reflected in the lowering of the hydrogen plateau pressure which improves the prospects for charging efficiency and charge retention of the hydride electrode. This structural change due to substitution is also reflected in a decrease in the gas phase hydrogen storage capacity per formula unit (FU) and a reduced molar volume of hydrogen (V_H) The electrochemical performance characteristics of the metal hydride electrodes are given in Table 2. The results indicate that substitution of Sn for Ni in the $LaNi_5$ lattice significantly improves the hydride stability. This is consistent with the reduction in the gas phase hydrogen plateau pressure, and is in agreement with the recent results of Rathnakumar *et. al.*, (26). The results in Table 2 indicate that these materials containing Sn or Ce give a very significant improvement in the cycle life relative to the $LaNi_5$. From these results it is clear that the substitution of the AB_5 type alloys with small amounts of Sn and Ce causes significant changes in both gas phase as well as the electrochemical characteristics of these alloys.

EXAFS Results: Figure 1 shows representative plots of the raw EXAFS data for $LaNi_5$ and $LaNi_{4.8}Sn_{0.2}$ respectively. Figure 2 shows a comparison of Fourier transforms of the EXAFS at the Ni K edge (Δ *k* ranges in Table 3) for the dry uncharged $LaNi_5$, $LaNi_{4.8}Sn_{0.2}$ and $La_{0.8}Ce_{0.2}Ni_{4.8}Sn_{0.2}$ electrodes. The results are almost identical. This is to be expected since all alloys have the hexagonal $CaCu_5$ structure. Detailed structural analysis using neutron diffraction show that there are two Ni sites, Ni_I and Ni_{II}, in $LaNi_5$ (27). The Ni_I atoms are in the basal plane (containing both Ni and La atoms) and are surrounded by six Ni_{II} atoms (3 each above and below) at a distance of 2.461 Å. Within the basal plane each Ni_I is surrounded by three Ni_I atoms at a distance of 2.896 Å and three La atoms at a distance of 2.896 Å. The Ni_{II} exist in a plane that consists exclusively of Ni atoms and are surrounded by four Ni_I atoms at a distance of 2.461 Å, four Ni_{II} atoms at a distance of 2.508 Å and four La atoms at a distance of 3.202 Å. The changes induced by substituting Ce or Sn in the lattice are due mainly to changes in the backscattering amplitude from the Sn and distortions in the coordination symmetry. These apparently are minimal as evidenced from the Fourier transforms of the EXAFS shown in Figure 2. The absence of a Ni-O contribution below 1.6 Å indicates that no significant oxidation of Ni occurred during electrode preparation.

Figure 3 shows that the substitution of Sn for some of the Ni causes a small change in the La L_{III} EXAFS. The Fourier transform window of the isolated EXAFS (Table 3) was however limited in range due to the presence of La L_{II} edge, 400 eV beyond the L_{III} edge. In the case of $La_{0.8}Ce_{0.2}Ni_{4.8}Sn_{0.2}$, such an analysis was impossible because of the presence of the Ce L_{III} edge at 240 eV beyond the La L_{III} edge. In $LaNi_5$ each La atom is surrounded by six La atoms in the basal plane at a distance of 5.01 Å and two La atoms in the *c* direction at a distance of 3.98 Å. In addition each La atom is surrounded by six Ni_I atoms at a distance of 2.896 Å and twelve Ni_{II} atoms at a distance of 3.202 Å. The changes in the La EXAFS on the addition of Sn may be due to a reduction in the contribution of the Ni_{II} atoms because of the expansion along the *c* axis (28). This could account for the shift in the peak to lower *r* values. Once again there is no evidence for any significant oxidation of the La during electrode preparation.

In order to obtain structural parameters as a function of Sn and Ce substitution a detailed EXAFS analysis was attempted at the Ni K-edge for all the three alloys in their dry uncharged state. The windows in k and r space used to obtain the corresponding forward and inverse Fourier transforms for the three samples as well as the reference standards are given in Table 3 & 4. The structure of $LaNi_5$ and the expected EXAFS phase shifts indicate that the inverse Fourier transform will contain contributions from three Ni-Ni and two Ni-La shells. These are listed in Table 5. Unique solutions for the EXAFS analysis are impossible for a five shell fit. Also in the case of the other alloys it is impossible to extract information on the Ni-Ce or Ni-Sn interactions. The best that can be expected is that the EXAFS analysis will give qualitative information on the effects of addition of Sn and Ce. The approach taken was to fit the data to the most simple model that yielded a good fit. For all three alloys, the model consisted of two Ni-Ni and one Ni-La coordination shells. The result of the analysis is shown in Table 6. Figure 4 shows the representative plot for the three shell fit, in both k and r space for $LaNi_5$. The substitution of Sn for Ni causes an increase in all bond distances. This is consistent with the larger atomic radius for Sn (1.4 Å vs. 1.24 Å for Ni). The decreased Ni-La bond length for $La_{0.8}Ce_{0.2}Ni_{4.8}Sn_{0.2}$ is consistent with the smaller Ce atomic radius (1.72 Å vs. 1.88 Å for La). The increase in the Ni-Ni Debye Waller factors for Sn containing alloys is consistent with the increases in bond lengths, and the disorder introduced by substituting Sn for Ni in the lattice. Similarly, the decrease in the Debye Waller factor for the Ni-La interaction in $La_{0.8}Ce_{0.2}Ni_{4.8}Sn_{0.2}$ is consistent with the decrease in the Ni-La bond length. Thus the calculated parameters from the data analysis are internally consistent and are in agreement with the X-ray diffraction results (Table 2). They also agree with previous X-ray and neutron diffraction results for $LaNi_5$ and $LaNi_{4.8}Sn_{0.2}$ (27,28).

A comparison of the results for $LaNi_5$ in Table 6 with those in Table 5 indicates some uncertainty in the bond distances determined by EXAFS. For one and two shell fits R can normally be determined to within ± 0.01 Å and N to within ± 15 %. In such complicated alloys the accuracies are reduced by at least a factor of three. The fact that the results of the substituted alloys could be fitted to a similar model indicates that it is unlikely that the substitution introduces any amorphous phases that cannot be detected by X-ray diffraction. It is also clear from the EXAFS that exposure of activated alloys to air does not result in any significant oxidation.

Significant changes occur in the Ni EXAFS during charge as shown by the representative plot for $LaNi_{4.8}Sn_{0.2}$ in Figure 5. These changes are similar to those observed by Suenobu *et al.*, in the gas phase, for amorphous $LaNi_5$ films (8,9).

Figure 6 shows a comparison of the Fourier transform of the Ni EXAFS for an uncycled dry $La_{0.8}Ce_{0.2}Ni_{4.8}Sn_{0.2}$ electrode and an electrode after 25 cycles, thus demonstrating the usefulness of the technique in detecting corrosion. The decrease in the peak at 2.0 Å and the appearance of a new peak at 1.5 Å indicates some corrosion of Ni to form $Ni(OH)_2$ for the electrode cycled 25 times ($\Delta k = 2.83 - 15.60$). Because of the contribution of several elements to the peak at 2.0 Å, phase correction techniques could not be used to separate the Ni-O contribution (15). The data were analyzed by simply doing a backtransform (Δr = 0-1.6 Å), and

using phase and amplitude parameters from a β-$Ni(OH)_2$ standard. This yielded an oxygen coordination number of 0.36 and a Ni-O bond distance of 1.96 Å, which is very close to that expected in $Ni(OH)_2$. In $Ni(OH)_2$ the coordination number is six. This indicates that about 6% of the Ni had corroded in 25 cycles. The result shows the power of the XAS technique to probe the corrosion of the alloy constituents because of its element specificity. No Ni corrosion products could be detected by X-ray diffraction presumably because of the amorphous nature of the $Ni(OH)_2$. Because of the complexity of the structure, the use of EXAFS in the study of major components in these alloys is of limited value. However, it is ideally suited for the study of environment around minor constituents. Furthermore, it is a very powerful technique for studying the corrosion of each of the individual components of the alloys during cycling. The XANES, however, yields very useful electronic information on the alloys.

XANES Results at the Ni K-Edge: Figure 7 shows normalized Ni K edge XANES spectra for the three dry uncycled electrodes. The edge is shifted by about 1.5 eV below that found for Ni foil. Substitutions by Ce and Sn decrease the peak at 0.0 eV. Absorption at the K edge is due to the excitation of *1s* electrons. Because of the selection rules only transitions into empty *4p* states are dipole allowed. In systems with cubic or octahedral symmetry the weak quadrupole allowed transitions are observed as small pre-edge peaks in the XANES (29). In the hexagonal symmetry of the alloys there is mixing of *p* and *d* states and as a result, transitions into empty *p* part of these mixed *p-d* states can occur. Theoretical calculations of the density of states (DOS) by Gupta (30) have shown that the Fermi level of $LaNi_5$ falls in a rapidly decreasing portion of the Ni *d* bands which are not fully filled. Thus the intensity of the peak at 0.0 eV can be taken as an indirect measure of the number of empty Ni *d* states. The reduction in the intensity of this peak on the addition of Sn and Ce is due to either a partial filling of the Ni *d* states, a reduction in symmetry by lattice distortion, or both. Filling of the Ni *d* bands could account for the reduction in the hydrogen storage capacity and the decrease in the plateau pressure of the substituted $LaNi_5$ alloys.

Figures 8-10 compares *in situ* Ni XANES for the three alloys in the charged state with that found for the dry uncharged electrode. The data for the dry uncharged electrode and a discharged electrode in the cell were identical. The results are very similar to those found by Suenobu *et al.* for amorphous $LaNi_5$ films (8,9). On hydriding, the Ni edge is shifted to coincide with that for the Ni foil. The theoretical calculations of Gupta (30) show that in $LaNi_5H_7$, the Ni *d* states are below the Fermi level and are narrowed. The mixed *p-d* states are no longer available for the excited *1s* electrons, hence the shift in the edge on the ingress of hydrogen.

Figure 11 compares the Ni XANES for an uncycled $La_{0.8}Ce_{0.2}Ni_{4.8}Sn_{0.2}$, a cycled electrode and for β-$Ni(OH)_2$. The appearance of a small white line in the cycled material signifies some Ni corrosion. A comparison of the area under the white line with that found for β-$Ni(OH)_2$ indicates that about 7% of the Ni has corroded. Thus, the results of the EXAFS and XANES are in good agreement.

XAS Results at the La L_3 Edge: Figure 12 shows the effect of the alloying substituents on the La L_3 XANES. The addition of Sn and Sn combined with Ce causes considerable increases in the white line. The transitions at the La L_3 edge are due to the excitation of $2p_{3/2}$ into the La *5d* states. Additions of Ce and Sn in the basal plane either increases the number of empty La *d* states or shifts their energy position with respect to the Fermi level.

Figures 13-15 show the *in-situ* La L_3 edge XANES for the three metal hydride electrodes as a function of electrochemical hydriding and dehydriding. As evident from these figures, the electrochemical hydriding causes a further depletion in the La *5d* orbital vacancy. This is evident from the increase in the magnitude of the white line as a result of hydriding. The calculations of Gupta showed that in $LaNi_5$ the nature of the *d* states at the Fermi level are largely nickel like with no lanthanum contribution (30). However, her calculations show that in $LaNi_5H_7$ the DOS right above the Fermi level is mostly from the *d* orbitals of La. The present results support this conclusion.

In-situ XAS Results at the Ce L_3 Edge: Figure 16 shows that hydriding has remarkable effects on the Ce L_3 XANES for $La_{0.8}Ce_{0.2}Ni_{4.8}Sn_{0.2}$. This effect is similar to that observed by Garcia *et al.* for $CeRu_2$ and $CeFe_2$ in the gas phase (7). Ce is unusual in that the energy of the inner 4 *f* level is nearly the same as the outer 5 *d* and 6 *s* levels (31). Thus small changes in energy and the environment around the Ce can change the relative occupancy of these atomic levels. This has been the subject of an enormous amount of publications in the physics literature and several reviews (31-33). At ambient temperature the two main allotropes are α-Ce and γ-Ce. Both have fcc structure with respective lattice constants of 4.83 Å and 5.15 Å. The γ state has a $4f^1 5d^1$ configuration and the α state has a mixed $4f^1 5d^1$ / $4f^0 5d^2$ configuration. This is reflected in the Ce L_{III} XANES where γ Ce has a spectrum similar to Ce (III) and α Ce has a spectrum similar to Ce (IV). The present results indicate that in the unhydrided alloy the Ce is in an α-like configuration similar to that found for $CeNi_5$ (32). On charging, the Ce becomes γ-like. Capehart *et al.* have done XAS studies on Ce_2Fe_{17}, $Ce_2Fe_{14}B$ and $CeFe_{14}BH_x$ alloys and concluded that the volume of the rare earth site was the principal factor controlling the electronic configuration about the Ce, with an expanded lattice favoring γ-like Ce (34). Hence lattice expansion as a result of hydriding causes the α-like Ce to convert to the γ form. The XANES results for the discharged electrode after 25 cycles indicates that there is some corrosion of Ce. The predominance of the low energy peak indicates that the corrosion product is largely trivalent Ce.

Conclusions

This study clearly demonstrates that *in situ* XAS is a very useful tool for the study of complex metal hydride materials since it provides both electronic and structural information. The element specific nature of the probe makes it very useful for elucidating the role of minor constituents and the corrosion of individual components.

(a) The XRD analysis result shows the effect of substitution of Ni by Sn causes an increase in the lattice parameters primarily along the c axis. This manifests itself in a

corresponding increase in the unit cell volume. Substitution of La by Ce however causes a minor contraction in the cell volume.

(b) The XANES results at the Ni K edge indicates that the alloying process results in hybridization of the 4*p* and 3*d* orbitals of Ni. The addition of Sn and Ce apparently decreases the number of Ni *d* band vacancies. This could account for both the decrease hydrogen content and the reduced plateau pressure.

(c) All of the XANES results at the Ni K and the La L_3 edge support the theoretical calculations of Gupta for $LaNi_5$ and $LaNi_5H_7$ (30).

(d) Both XANES and EXAFS confirm that about 6% of the Ni in $La_{0.8}Ce_{0.2}Ni_{4.8}Sn_{0.2}$ corrodes after 25 cycles.

(e) XANES results at the Ce L_3 edge indicate that hydriding causes Ce to convert from an α to a γ like state. Results on cycled electrodes indicate corrosion of Ce with a predominance of Ce (III) in the corrosion product.

References

(1) J. J. Reilly in Hydrogen Storage Materials, Batteries and Electrochemistry, (D. A. Corrigan and S. Srinivasan, Eds.,) The Electrochemical Society Inc., 92-5, 24, (1992).

(2) A. Anani, A. Visintin, S. Srinivasan, A. J. Appleby and H. S. Lim, J. Electrochem. Soc. 137, 985, (1992).

(3) M. P. S. Kumar, K. Petrov, W. Zhang, A. A. Rostami, S. Srinivasan, G. Adzic, J. R. Johnson, J. J. Reilly and H. S. Lim, Extended Abstracts, 185th Meeting of the Electrochemical Society, San Francisco, 94-1, 1225, (1994), p. 1225.

(4) M. Gupta, L. Schlapbach in Hydrogen in Intermetallic Compounds I, (L. Schlapbach, Ed.) Topics in Physics Series, Springer Verlag, Volume 63, (1988), p. 139.

(5) K. Tanaka, C. Sugiura, S. Nakai and Y. Ohno, Jpn. J. App. Phys, 20, 41 (1981).

(6) B. Lengeler and R. Zeller, J. of the Less Common Metals 103, 337 (1984).

(7) J. Garcia, J. Bartolome, M. S. del Rio, Zeitschrift fur Physikalische Chemie Nue Folge, Bd. 163, S. 277 (1989).

(8) T. Suenobu, H. Sakaguchi, T. Tsuji, H. Kanai, S. Yoshida and G. Adachi, Bull. Chem. Soc. Jpn. 64, 3522 (1991).

(9) T. Suenobu, H. Sagakuchi, G. Adachi, H. Kanai and S. Yoshida, J. of Alloys and

Compounds 190, 273 (1993).

(10) D. A. Tryk, I. T. Bae, Y. Hu, S. Kim, M. R. Antonio and D. A. Scherson, J. Electrochem. Soc. 142, 824 (1995).

(11) J. J. Reilly and R. H. Wiswall, Inorg. Chem. 9, 1968 (1970).

(12) G. D. Adzic, J. R. Johnson, J. J. Reilly, J. McBreen, S. Mukerjee, M. P. S. Kumar, W. Zhang and S. Srinivasan, Proceedings of the Symposium on Electrochemistry and Material Science of Cathodic Hydrogen Absorption and Adsorption, B. E. Conway and G. Jerkiewicz, Eds., The Electrochemical Society Inc., Pennington, NJ (1994).

(13) J. McBreen, W. E. O'Grady, K. I. Pandya, R. W. Hoffman and D. E. Sayers, Langmuir 3, 418 (1987).

(14) S. Mukerjee, S. Srinivasan, M. P. Soriaga and J. McBreen, J. Electrochem. Soc. 142, 1409 (1995).

(15) K. I. Pandya, R. W. Hoffman, J. McBreen and W. E. O'Grady, J. Electrochem. Soc. 137, 383 (1990).

(16) J. J. Reilly, in Inorganic Synthesis, S. L. Holt, Ed., J. Wiley & Sons, New York, 1983, p. 90.

(17) M. H. Mendelsohn, D. M. Gruen and A. E. Dwight, ibid., p.96.

(18) D. E. Sayers, D. A. Bunker, in X-ray Absorption: Principles, Applications, Techniques of EXAFS, SEXAFS and XANES, (D. C. Koningsberger and R. Prins, Eds.,) John Wiley and Sons, New York (1988), pp. 211.

(19) J. Wong, F. W. Lyttle, R. P. Messner, D. H. Maylotte, Phys. Rev. B 30, 5596 (1984).

(20) J. B. A. D. vanZon, D. C. Koningsberger, H. F. I. vant'Blik and D. E. Sayers, J. Chem. Phys. 82, 5742 (1985).

(21) F. B. M. Duivenvoorden, D. C. Koninsberger, Y. S. Oh and B. C. Gates, J. Am. Chem. Soc. 108, 6254 (1986).

(22) K. I. Pandya, W. E. O'Grady, D. A. Corrigan, J. McBreen and R. W. Hoffman, J. Phys. Chem. 94, 21 (1990).

(23) M. Vaarkamp, I. Dring, R. J. Oldman, E. A. Stern and D. C. Koningsberger, Phys. Rev. B 50, 7872 (1994)

(24) P. H. Citrin, P. Eisenberger and B. M. Kincaid, Phys. Rev. Lett. 36, 1346 (1976).

(25) J. J. Rehr, J. Mustre de Leon, S. I. Zabinski and R. C. Albers, J. Am., Chem., Soc. 113, 5135 (1991).

(26) B. V. Rathnakumar, C. Witham, B. Fultz and G. Halpert, J. Electrochem. Soc. 141, L89 (1994).

(27) P. Thompson, J. J. Reilly, L. M. Corliss, J. M. Hastings and R. Hempelmann, J. Phys. F: Met Phys. 16, 675 (1986).

(28) J. S. Cantrell, T. A. Beiter and R. C. Bowman Jr., J. of Alloys and Compounds 207-208, 372 (1994).

(29) A. N. Mansour, C. A. Melendres, M. Pankuch and R. A. Brizzolara, J. Electrochem. Soc. 141, L69 (1994).

(30) M. Gupta, J. of the Less Common Metals 130, 219 (1987).

(31) D. C. Kosenmaki and K. A. Gschneidner, Jr., Handbook on the Physics and Chemistry of Rare Earths, K. A. Gschneidner, Jr., and L. Eyring, Eds. North Holland, Amsterdam (1978), pp. 337-377.

(32) D. Wohlleben and J. Rohler, J. Appl. Phys. 55, 1904 (1984).

(33) G. Krill, J. Phys., C8, 907 (1986).

(34) T. W. Capehart, R. W. Mishra, G. P. Meisner, C. D. Fuerst and I. F. Herbst, Appl. Phys. Lett. 63, 3642 (1993).

(35) J. J. G. Willems, Phillips J. Res., 39, 1 (1984).

Table 1

Physico-chemical Properties of Modified AB_5 Type Alloys

Composition	Lattice Parameters		Cell Volume	Plateau Pressure[a]	H_{max}/FU	V_H
	a, Å	c, Å	$(Å)^3$	atm.		$(Å)^3$
$LaNi_5$	5.009	3.970	86.31	1.80	6.90	3.5[b]
$LaNi_{4.8}Sn_{0.2}$	5.0557	4.019	88.96	1.01	6.26	3.2
$La_{0.8}Ce_{0.2}Ni_{4.8}Sn_{0.2}$	5.033	4.038	88.6	1.08	5.73	-

(a) All reported values are at a temperature of 299°K
(b) Obtained from ref., (34)

Table 2

Performance Characteristics of Hydride Electrodes with Modified AB_5 Type Alloys

Composition	Initial Capacity mAh/gm	Discharge Potential mV(Hg/HgO)	Rate Capability 1C/3C[a] (%)	Decay Rate mAh/gm cycle
$LaNi_5$	350[b]	-	-	45%[b],[c]
$LaNi_{4.8}Sn_{0.2}$	296	900	93	0.93
$La_{0.8}Ce_{0.2}Ni_{4.8}Sn_{0.2}$	315	935	83	0.77

(a) Ratio of capacity based on electrodes being charged and discharged at C and C/3 rate respectively.
(b) Obtained from ref., (34)
(c) After 100 cycles

Table 3

Fourier transformation ranges of the forward and inverse transforms (k^3 weighted) at the Ni k-edge for $LaNi_5$, $LaNi_{4.8}Sn_{0.2}$ and $La_{0.8}Ce_{0.2}Ni_{4.8}Sn_{0.2}$ as dry uncharged electrodes.

Composition	Δk ($Å^{-1}$)	Δr (Å)
$LaNi_5$	3.10-14.56 (2.46-9.87)*	1.38-2.56
$LaNi_{4.8}Sn_{0.2}$	3.80-15.26 (2.45-9.87)*	1.40-2.86
$La_{0.8}Ce_{0.2}Ni_{4.8}Sn_{0.2}$	3.85-15.16	1.24-2.94

*: Δk ranges for EXAFS data at the La L_{III} edge.

Table 4

Fourier transformation ranges of the forward and inverse transforms for the reference standards at the Ni k-edge.

Reference Standard	Δk ($Å^{-1}$)	Δr (Å)	N_{ref}	R_{ref}
Ni-Ni Standard Ni foil (Liq. N_2 Temp.)	3.45-15.24	1.10-2.80	12	2.492
Ni-La Standard (FEFF Program)	3.05-19.95	1.5-2.5	4	3.5

Table 5

Nickel coordination in $LaNi_5$

Coordination Shell	Coordination Number (Normalized Average)	Bond Distance (Å)
Ni-Ni (1)	4.8	2.461
Ni-Ni (2)	2.4	2.508
Ni-Ni (3)	1.2	2.896
Ni-La (1)	1.2	2.896
Ni-La (2)	2.4	3.202

Table 6

Result of EXAFS analysis at the Ni K edge for $LaNi_5$, $LaNi_{4.8}Sn_{0.2}$, and $La_{0.8}Ce_{0.2}Ni_{4.8}Sn_{0.2}$ dry uncharged electrodes.

Composition	Coordination Shell	EXAFS Parameter			
		N	R (Å)	$\Delta\sigma^2$ ($Å^2$)	ΔE_o (eV)
$LaNi_5$	Ni-Ni (1)	4.20	2.43	0.00200	-10.30
	Ni-Ni (2)	2.91	2.52	0.00008	-0.66
	Ni-La	2.63	3.17	0.01805	3.80
$LaNi_{4.8}Sn_{0.2}$	Ni-Ni (1)	4.80	2.50	0.00360	-2.15
	Ni-Ni (2)	4.00	2.74	0.01354	2.46
	Ni-La	3.10	3.35	0.00386	-4.35
$La_{0.8}Ce_{0.2}Ni_{4.8}Sn_{0.2}$	Ni-Ni (1)	4.30	2.50	0.00242	-4.95
	Ni-Ni (2)	4.15	2.76	0.01534	6.51
	Ni-La	1.42	3.13	-0.00617	-4.24

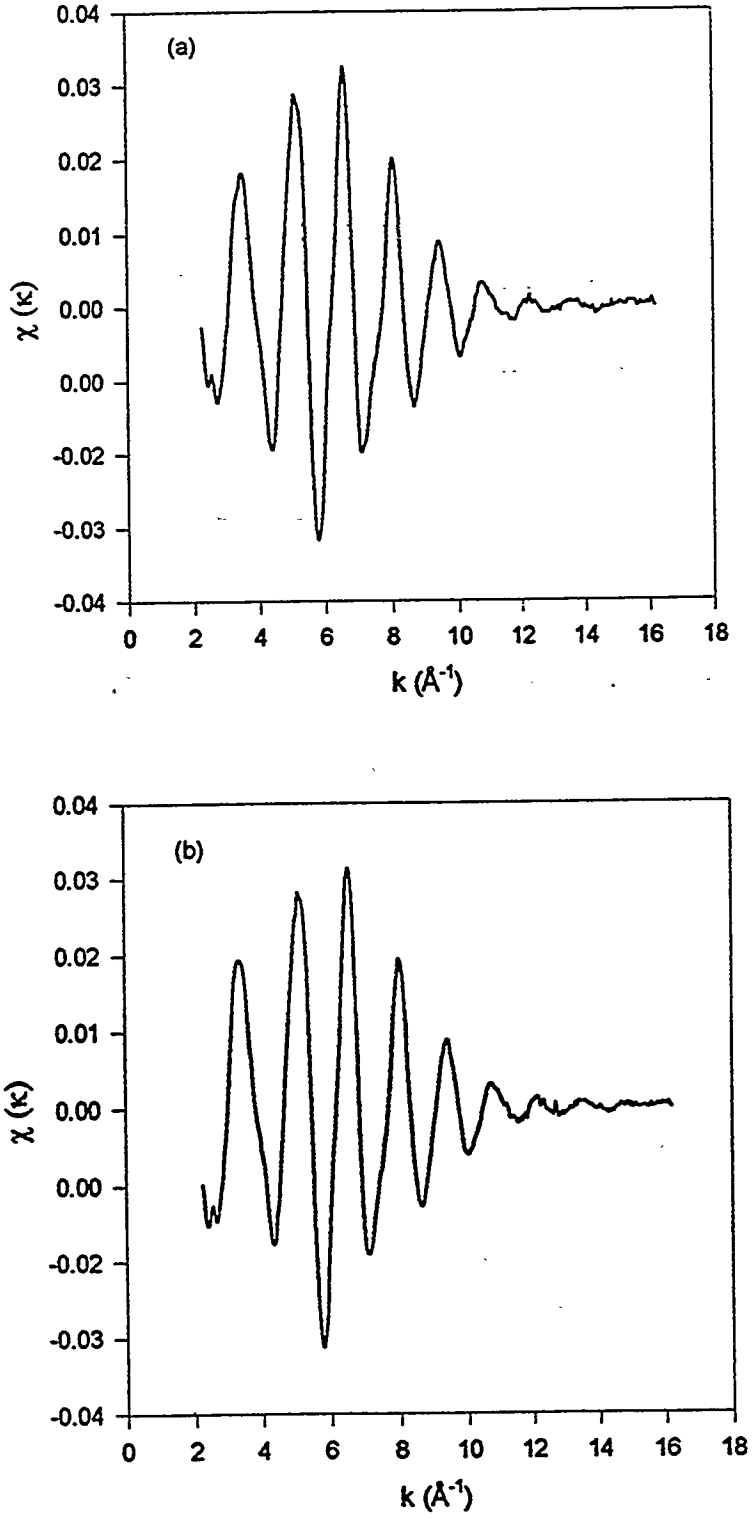

Figure 1. Ni EXAFS spectra for (a) $LaNi_5$ and (b) $LaNi_{4.8}Sn_{0.2}$ in dry uncharged electrodes.

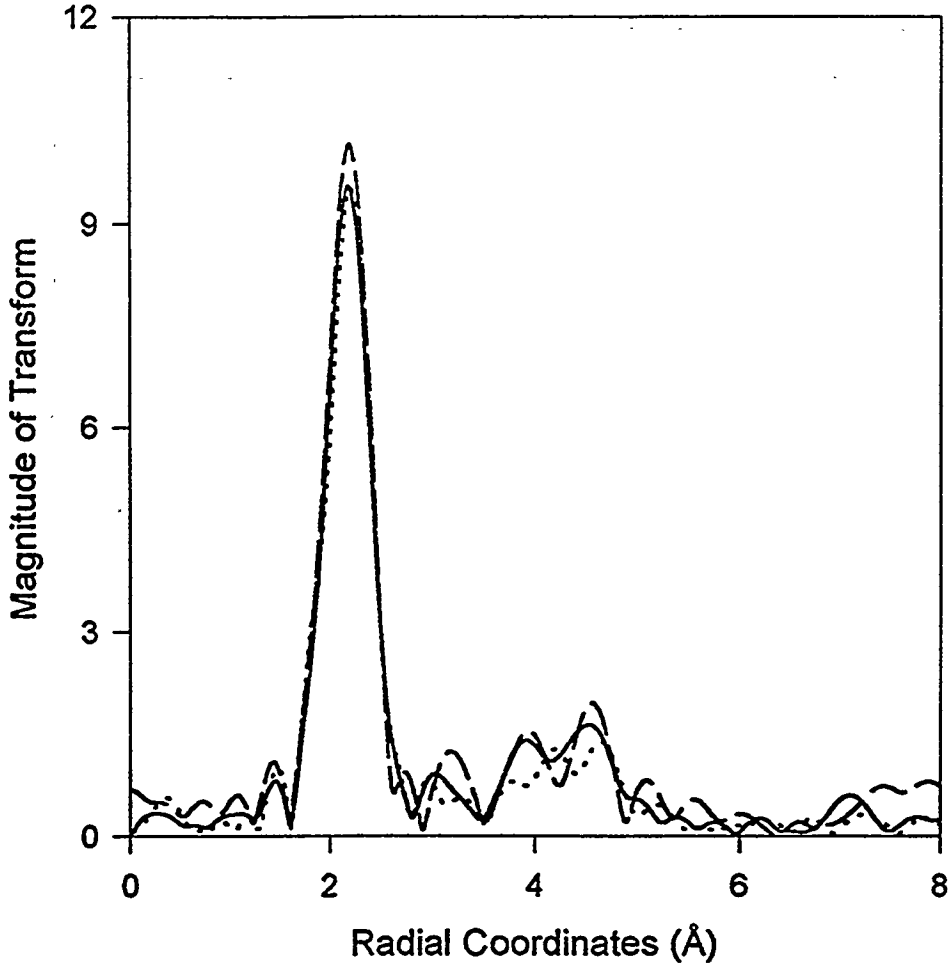

Figure 2. Comparison of the Fourier transforms of the EXAFS (k^3 weighted) at the Ni K-edge for $LaNi_5$ (—), $LaNi_{4.8}Sn_{0.2}$ (...) and $La_{0.8}Ce_{0.2}Ni_{4.8}Sn_{0.2}$.(---) in dry uncharged electrodes.

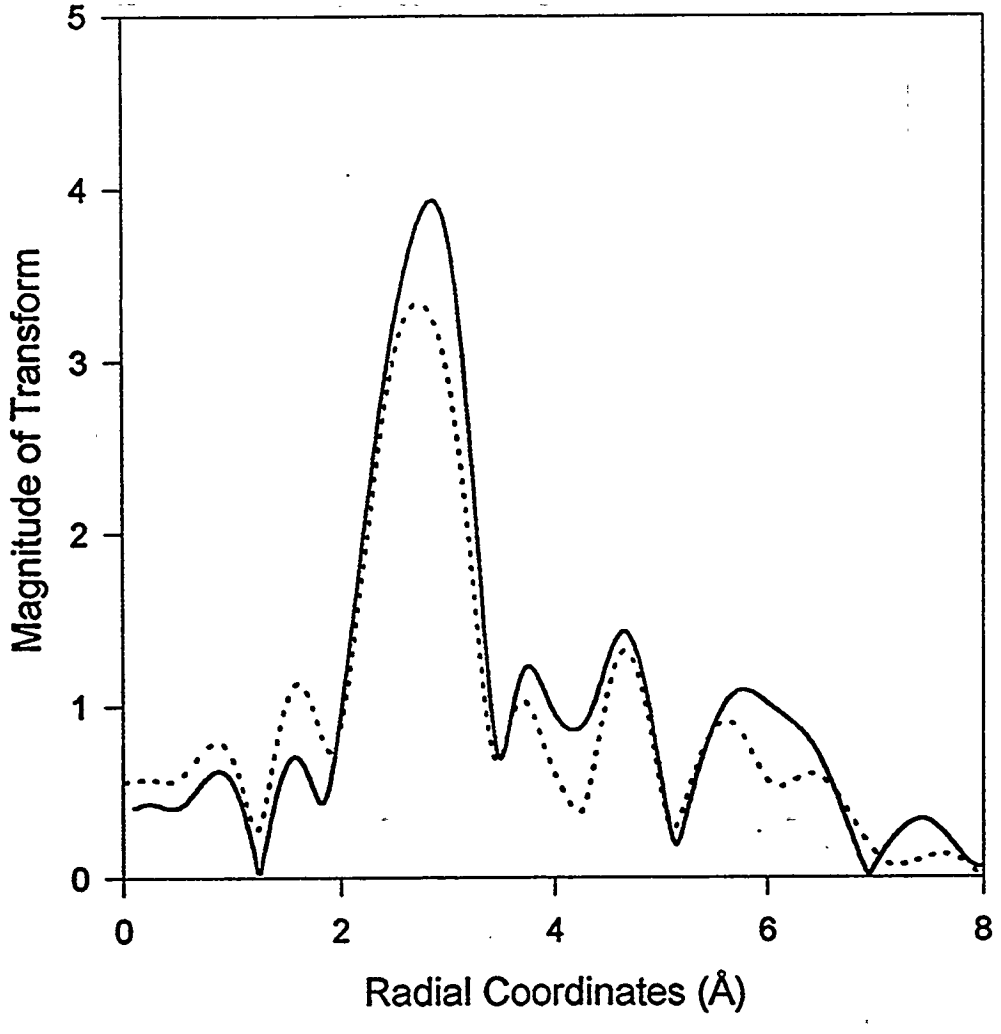

Figure 3. Comparison of the Fourier transforms of the EXAFS (k^3 weighted) at the La L_{III}-edge for $LaNi_5$ (—) and $LaNi_{4.8}Sn_{0.2}$ (...) in dry uncharged electrodes.

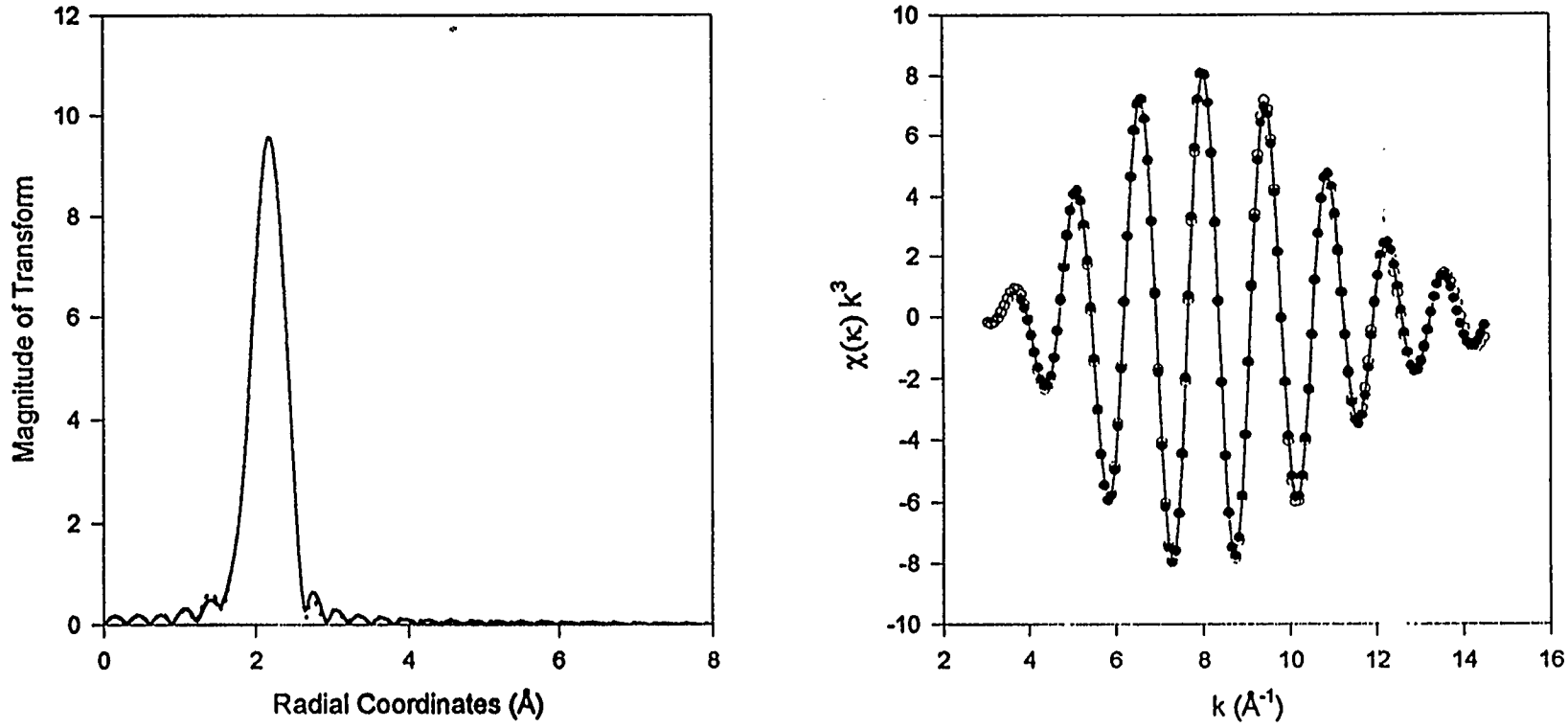

(a). (b)

Figure 4. A three shell fit of Ni EXAFS (k^3 weighted) for $LaNi_5$ in (a) *r* space, (...) experimental data and (—) fit and (b) *k* space, (O) .experimental data and (●) fit.

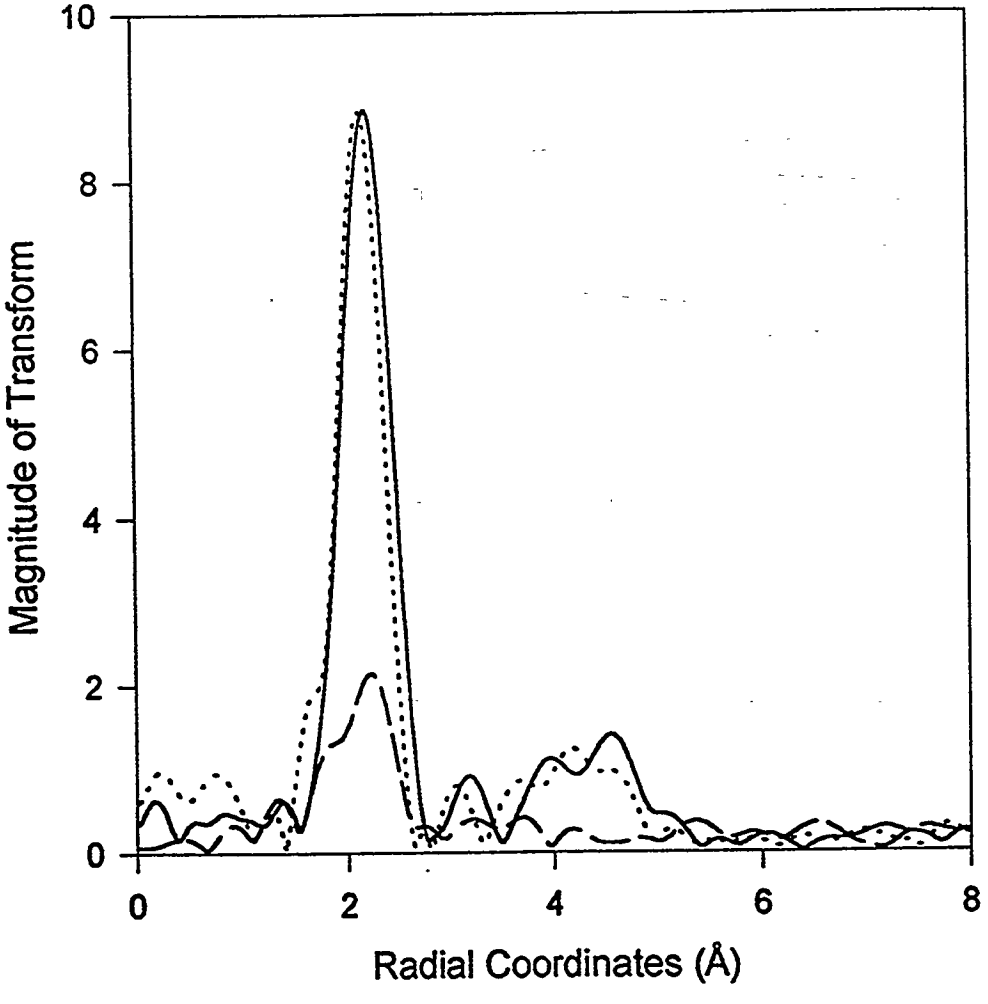

Figure 5. Comparison of Fourier transforms of the EXAFS (k^3 weighted) at the Ni K-edge for $LaNi_{4.8}Sn_{0.2}$ as a function of state of charge. $LaNi_{4.8}Sn_{0.2}$ dry *ex-situ* uncharged (—), *in-situ* charged (---) and *in-situ* discharged (...).

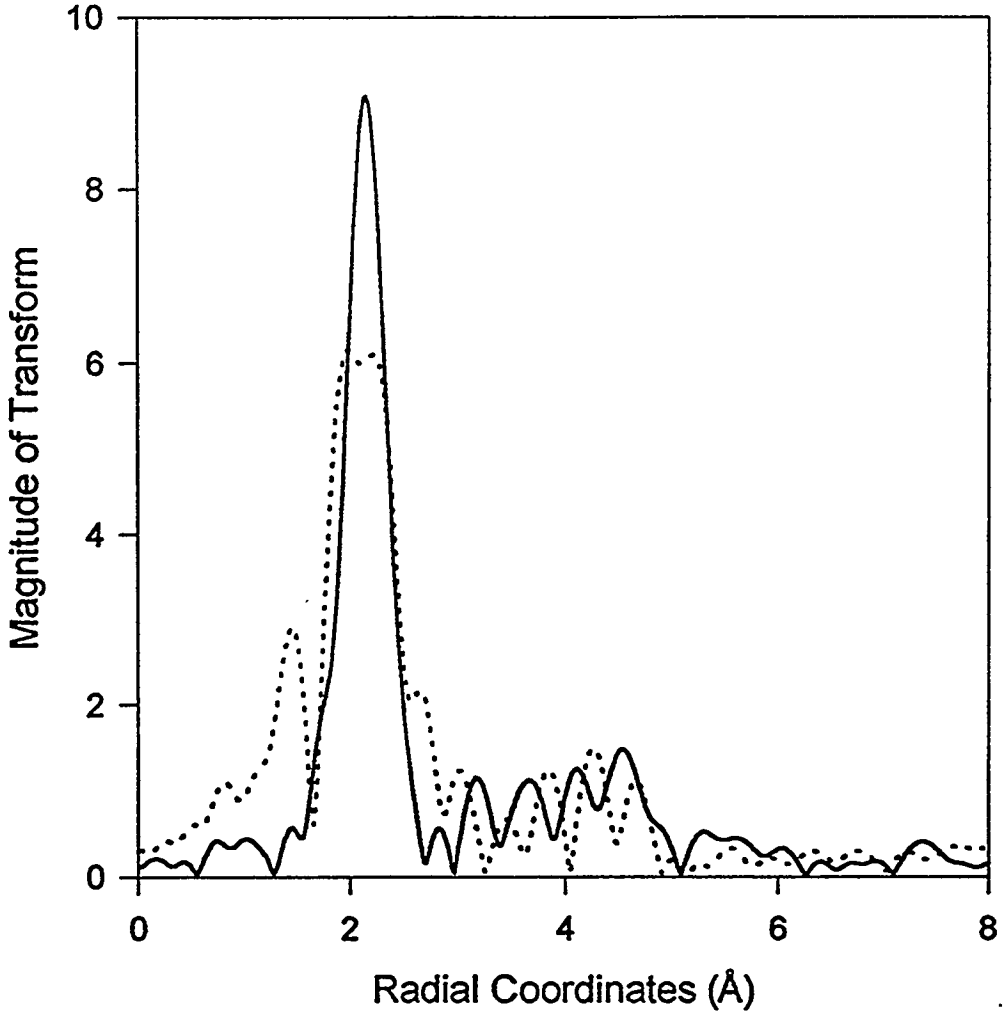

Figure 6. Fourier transforms of the EXAFS (k^3 weighted) at the Ni K-edge for $La_{0.8}Ce_{0.2}Ni_{4.8}Sn_{0.2}$. $La_{0.8}Ce_{0.2}Ni_{4.8}Sn_{0.2}$ dry uncharged electrode (—) and discharged (...) electrode after 25 cycles.

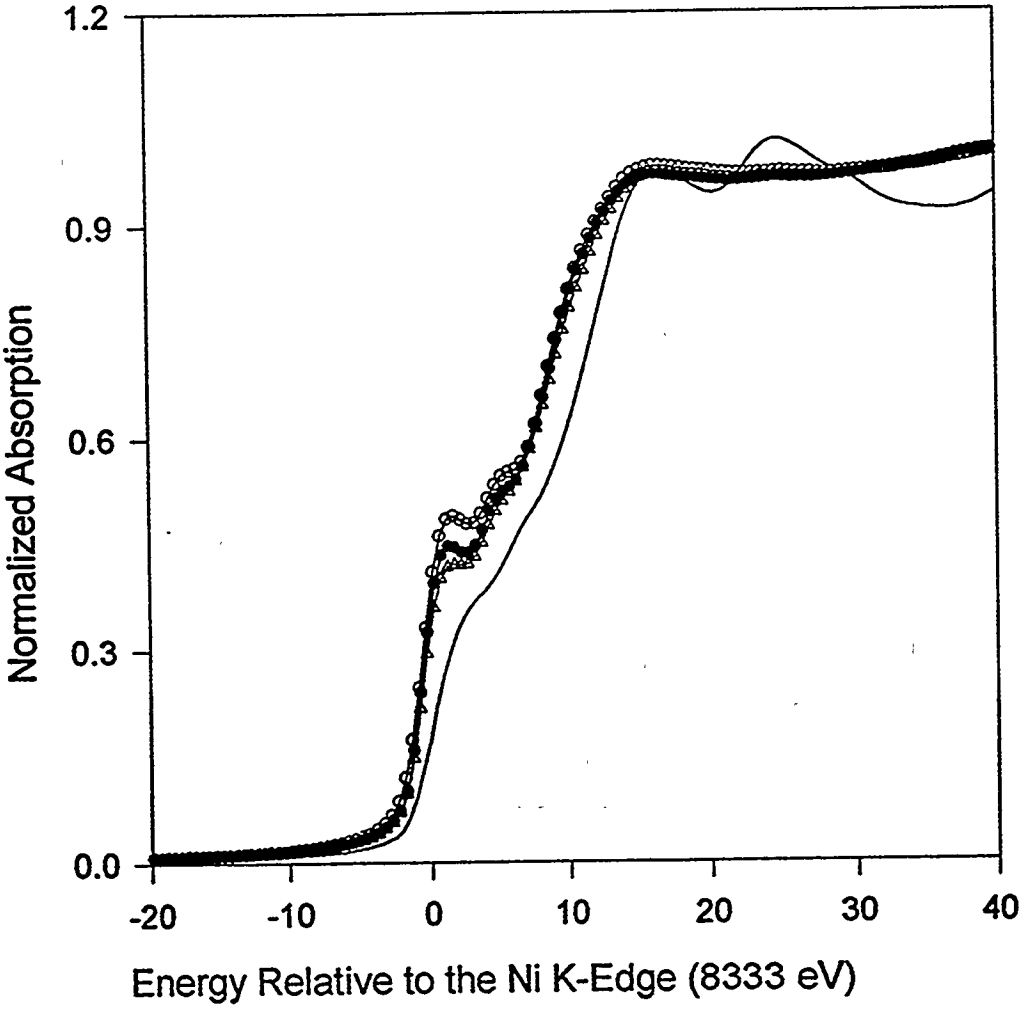

Figure 7. Comparison of the Ni K-edge XANES for $LaNi_5$ (O), $LaNi_{4.8}Sn_{0.2}$ (●) and $La_{0.8}Ce_{0.2}Ni_{4.8}Sn_{0.2}$ (Δ) in dry uncharged electrodes relative to the pure Ni foil (—) data.

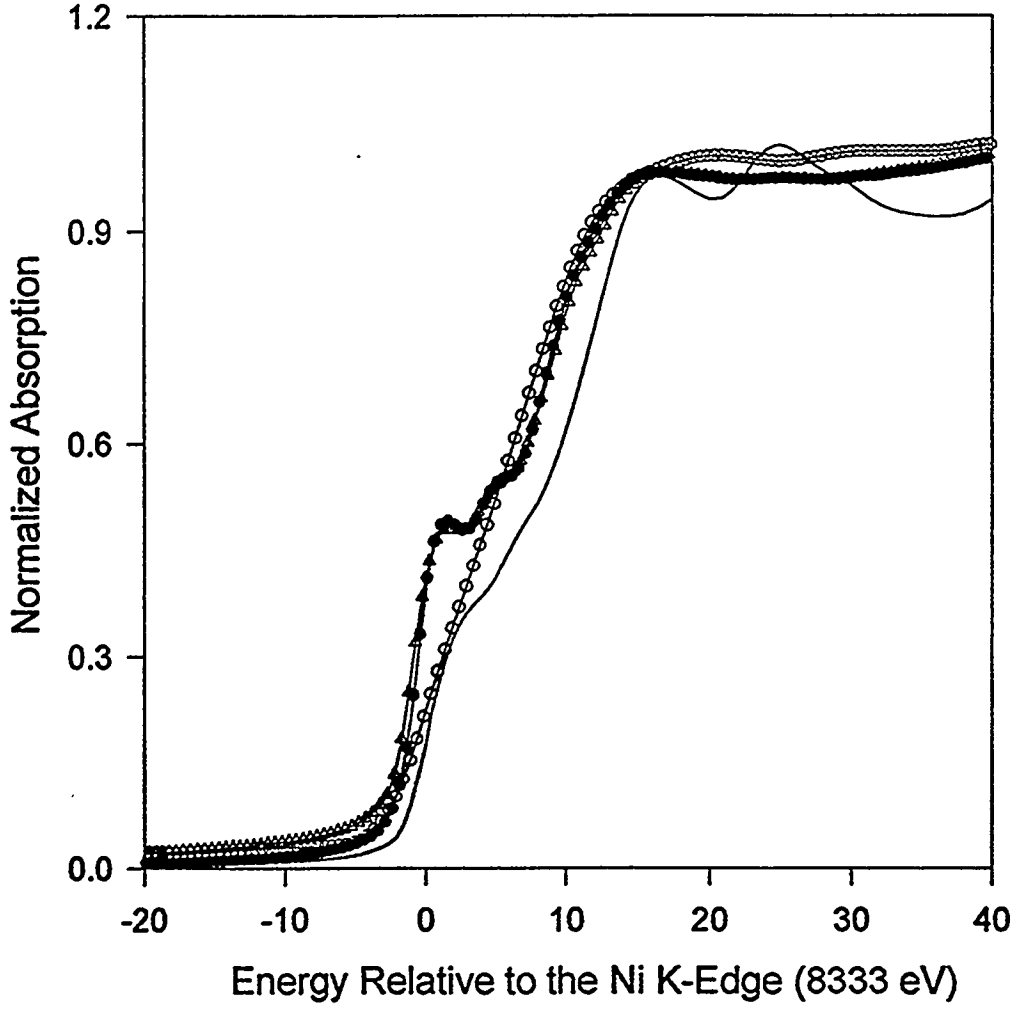

Figure 8. Comparison of Ni K-edge XANES spectra for $LaNi_5$ as a function of state of charge. Ni foil (—), $LaNi_5$ dry uncharged (●), *in-situ* charged (O) and *in-situ* discharged (Δ).

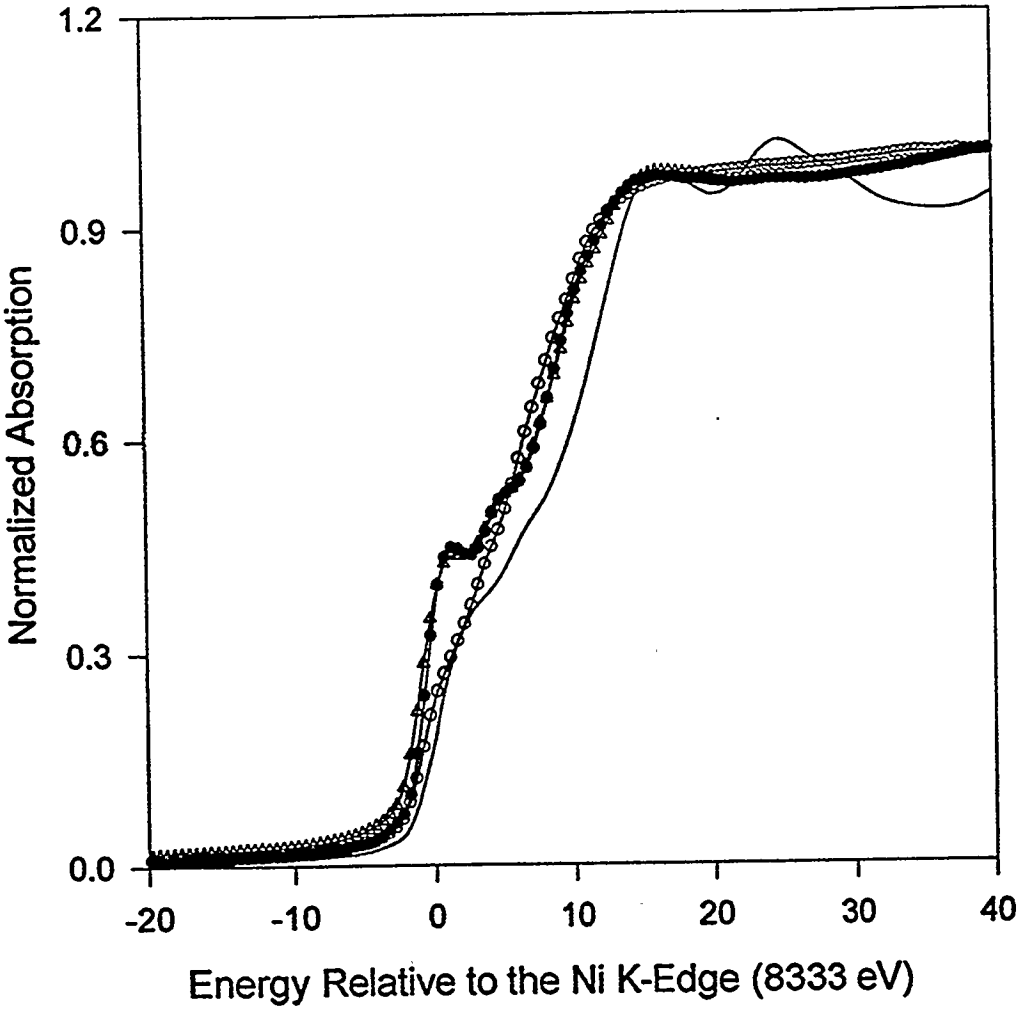

Figure 9. Comparison of Ni K-edge XANES spectra for $LaNi_{4.8}Sn_{0.2}$ as a function of state of charge. Ni foil (—), $LaNi_{4.8}Sn_{0.2}$ dry uncharged (●), *in-situ* charged (O) and *in-situ* discharged (Δ).

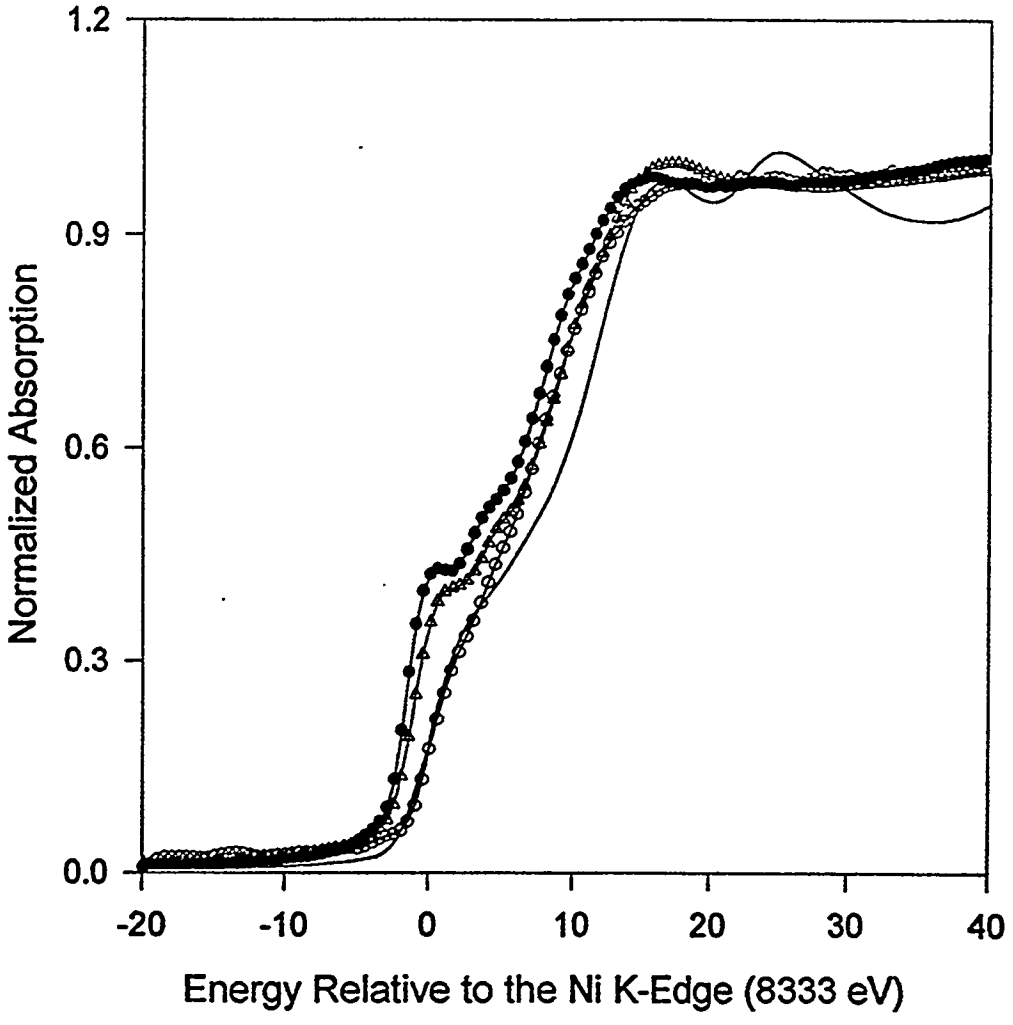

Figure 10. Comparison of Ni K-edge XANES spectra for $La_{0.8}Ce_{0.2}Ni_{4.8}Sn_{0.2}$ as a function of state of charge. Ni foil (—), $La_{0.8}Ce_{0.2}Ni_{4.8}Sn_{0.2}$ dry uncharged (●), *in-situ* charged (O) and *in-situ* discharged (Δ).

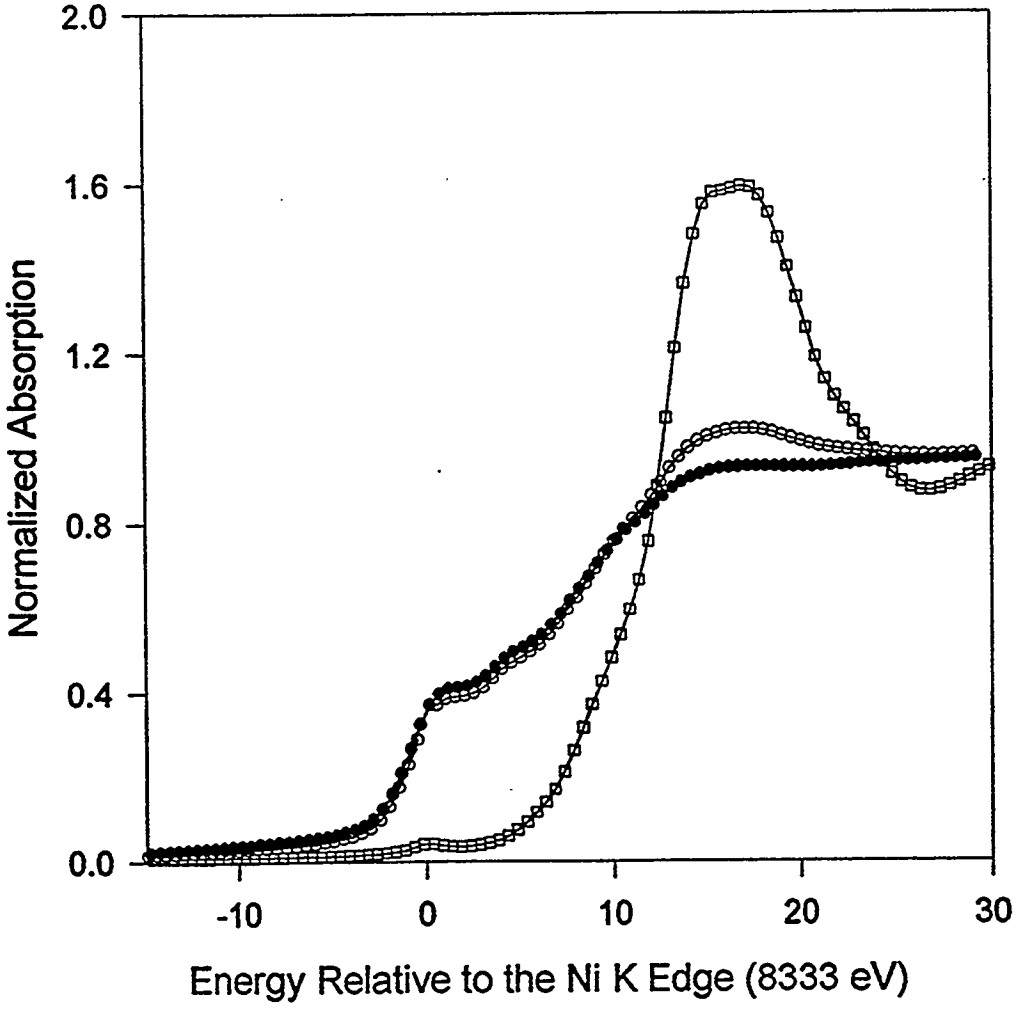

Figure 11. Ni K-edge XANES for $La_{0.8}Ce_{0.2}Ni_{4.8}Sn_{0.2}$ electrodes. $La_{0.8}Ce_{0.2}Ni_{4.8}Sn_{0.2}$ dry uncharged (●), *ex-situ* discharged after 25 cycles (O) and a β-$Ni(OH)_2$ reference standard (□).

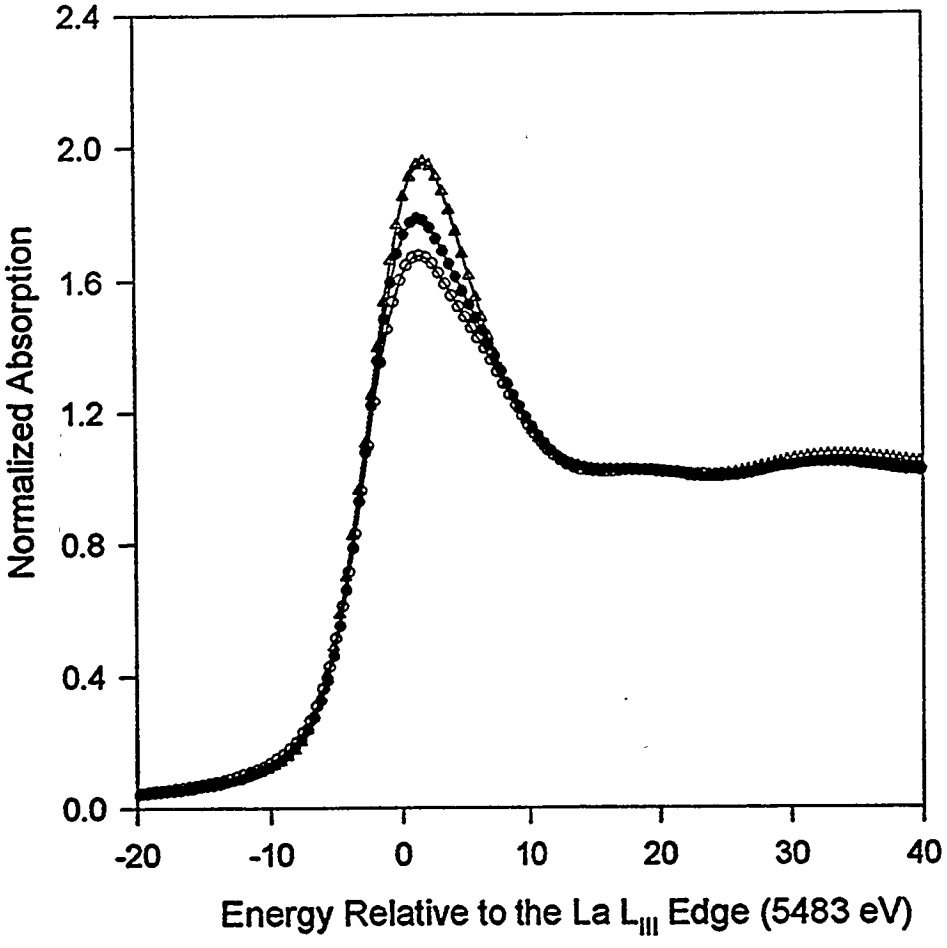

Figure 12. Comparison of the La L_{III}-edge XANES for $LaNi_5$ (O), $LaNi_{4.8}Sn_{0.2}$ (●) and $La_{0.8}Ce_{0.2}Ni_{4.8}Sn_{0.2}$ (Δ) in dry uncharged electrodes.

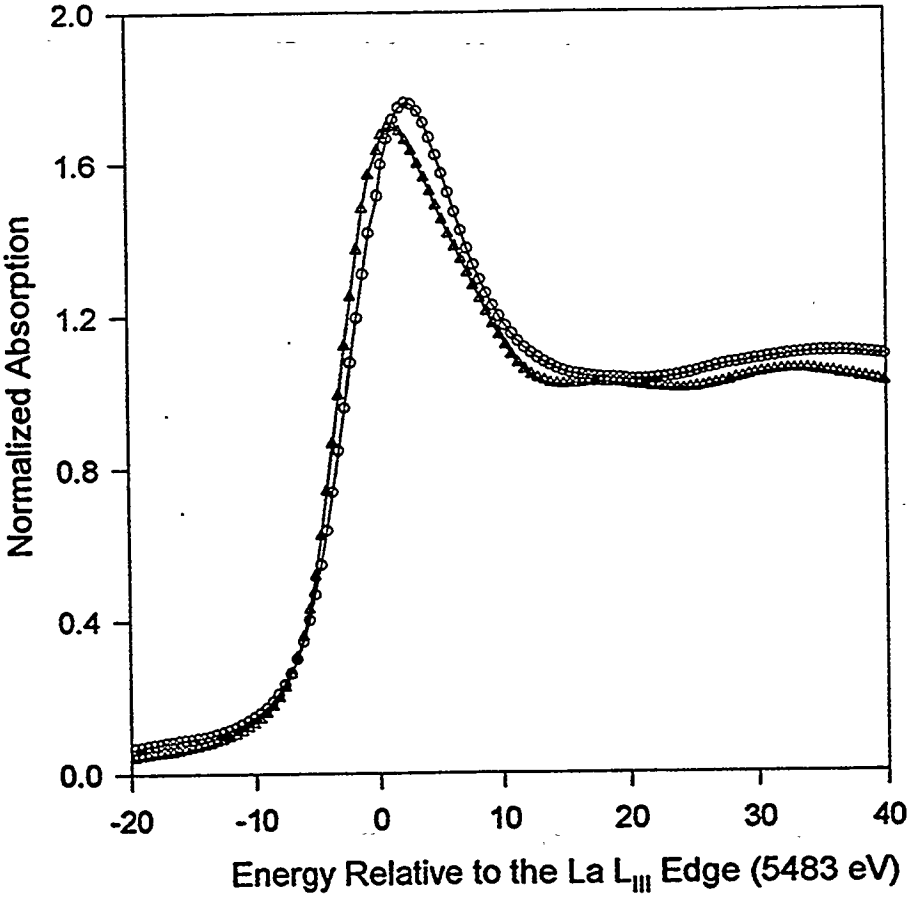

Figure 13. Comparison of *in-situ* La L_{III}-edge spectra for $LaNi_5$ as a function of state of charge. $LaNi_5$ charged (O) and discharged (Δ).

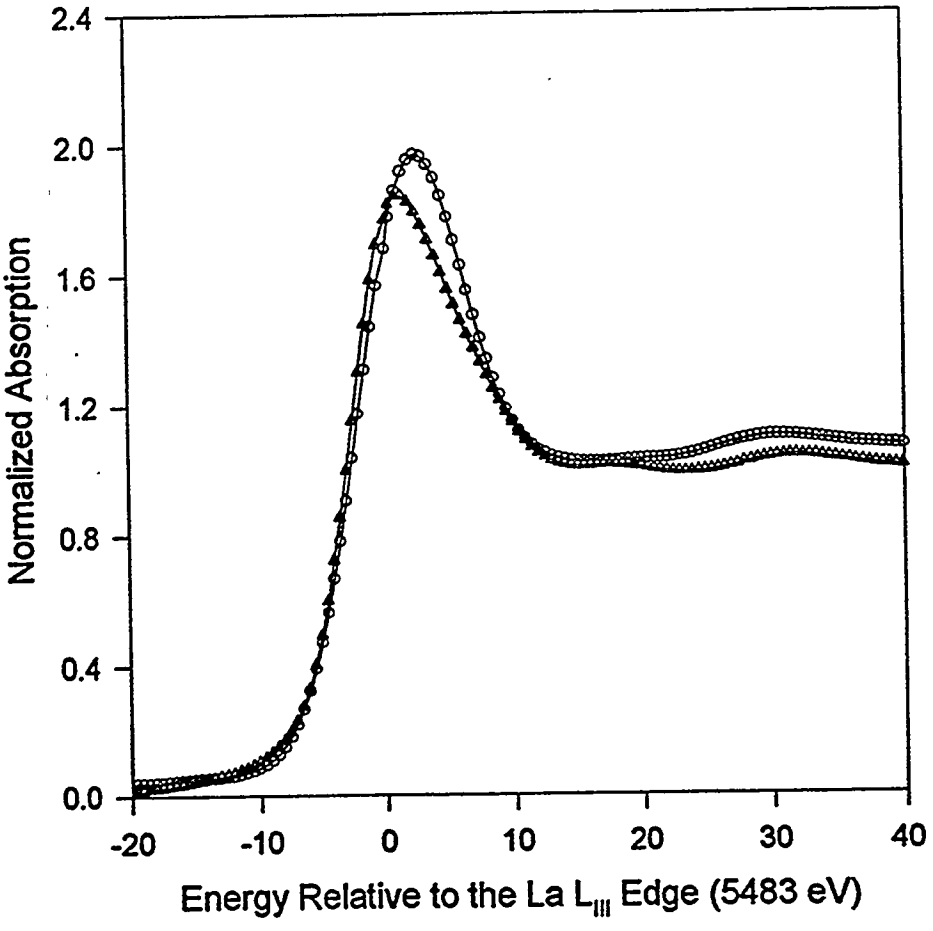

Figure 14. Comparison of *in-situ* La L_{III}-edge spectra for $LaNi_{4.8}Sn_{0.2}$ as a function of state of charge. $LaNi_{4.8}Sn_{0.2}$ charged (O) and discharged (Δ).

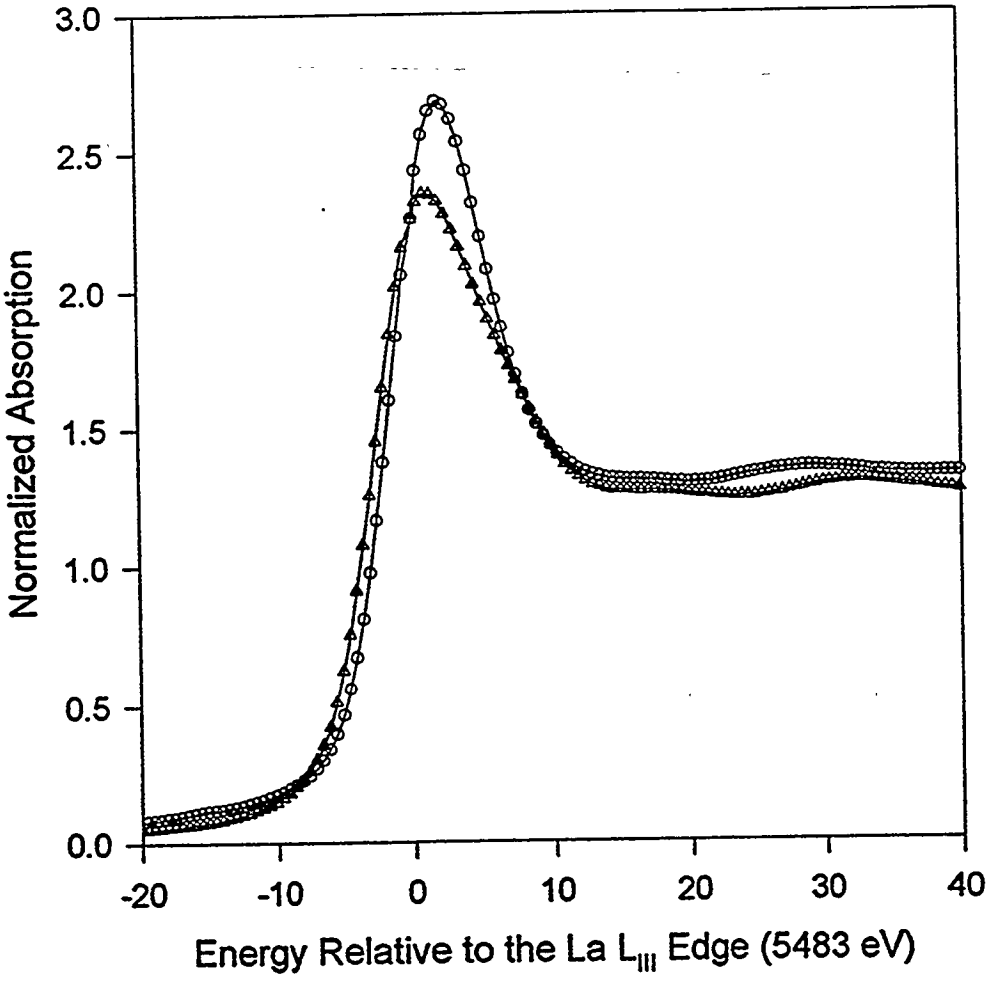

Figure 15. Comparison of *in-situ* La L_{III}-edge spectra for $La_{0.8}Ce_{0.2}Ni_{4.8}Sn_{0.2}$ as a function of state of charge. $La_{0.8}Ce_{0.2}Ni_{4.8}Sn_{0.2}$ charged (O) and discharged (Δ).

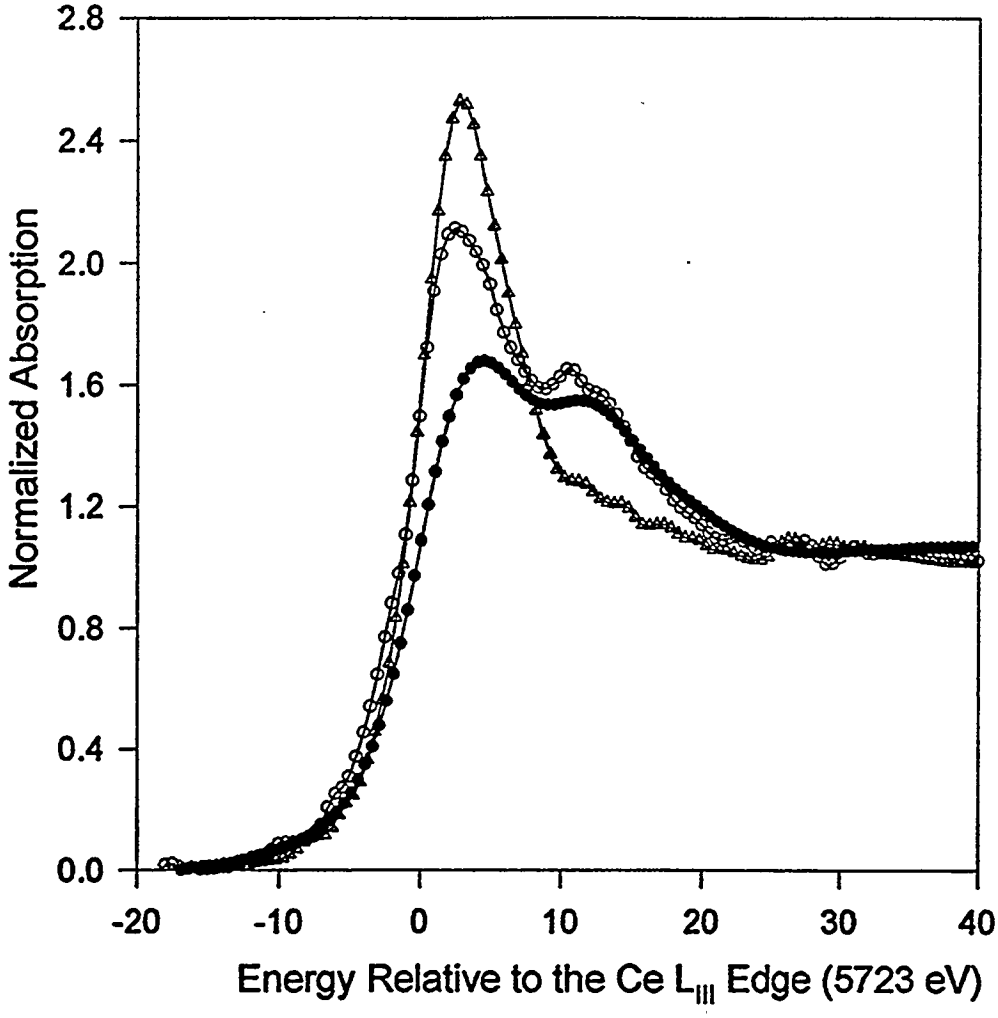

Figure 16. Comparison of Ce L_{III}-edge spectra for $La_{0.8}Ce_{0.2}Ni_{4.8}Sn_{0.2}$ as a function of state of charge and cycling. $La_{0.8}Ce_{0.2}Ni_{4.8}Sn_{0.2}$ dry uncharged (●), *in-situ* charged (Δ) and dry *ex-situ* discharged (O) after 25 cycles.

3. EFFECT OF Ce COMPOSITION ON THE STRUCTURAL AND ELECTRONIC CHARACTERISTICS OF SOME METAL HYDRIDE ELECTRODES: A XANES AND EXAFS INVESTIGATION

S.Mukerjee, J. McBreen, J. J. Reilly, J. R. Johnson and G. Adzic, BNL
M. P. S. Kumar, W. Zhang and S. Srinivasan, Texas A&M University

Introduction

Recent advances in the development of advanced nickel metal hydride alloys have resulted in it replacing cadmium as the anode in rechargeable alkaline batteries (1). Among the principle alloy types currently under consideration are the AB_2 and AB_5 type alloys. The hydrogen storage and electrochemical characteristics of these alloys depend intimately on their composition. Among the AB_5 type alloys, substitution of the prototype alloy $LaNi_5$ with small amounts of other alloying elements have shown improvements in terms of both electrochemical capacity as well as cycle life of the alloy material. A previous investigation (2) involving individual substitutions of Ni (in $LaNi_5$) with small amounts of Co, Al and Mn have shown their ability to improve the electrochemical capacity. These improvements have been attributed to the lowering of the hydrogen plateau pressure. Recent results with Sn substitution (3,4) and have shown similar effects and have attributed the lowering of the hydrogen plateau pressure to an increase in the lattice parameters (cell volume). Such Ni substitutions also result in the decrease of the capacity loss due to lower corrosion. This has been attributed (5) to the reduced alloy expansion and contraction in these alloys (lower hydrogen molar volume). Similar effects are also observed as a result of substitution of La with rare earth elements such as Ce. This is borne out by the good performance characteristics of mischmetal $(Mm)B_5$ battery electrodes, wherein the Mm contains (in atom %) 50-55% Ce, 18-28% La, 12-18% Nd, 4-6% Pr, <0.1% Sm and <2% others. However, little is known about the effect of Ce substitution in terms of its effect on the corrosion of individual alloying elements (particularly Ni) as a function of cycling.

X-ray absorption spectroscopy (XAS) can in principle elucidate both electronic and structural changes that occur on the substitution of alloy substituents and on the ingress of hydrogen into the alloy. The XAS spectra consists of two parts, the near edge part, XANES, which gives chemical information and the EXAFS which yields structural information. The X-ray absorption near edge structure (XANES, ± 50 eV relative to the absorption edge) comprises primarily of multiple scattering and transitions to empty states in the vicinity of the Fermi level by low energy photo-electrons with relatively long mean-free paths. The XANES can provide information on the oxidation state from the size and shift in the edge-transition, and on the coordination symmetry of ligands around the excited atom from the shape of the edge transition. The XANES probes empty states which are thought to be important in hydrogen storage (6). Due to its ability to probe empty states near the Fermi level it can provide important information on the extent of corrosion of individual components. The extended X-ray absorption fine structure (EXAFS) region is 40-1500 eV beyond the absorption edge and is caused by the modulation of the X-ray intensity due to back-scattering by a small fraction of the back-scattered photoelectron wave due to atoms surrounding the absorber. This interference effect caused by single-scattering

electrons with short mean-free paths provides information about the short-range atomic order (coordination number and bond distances).

Recent results (7) have shown the possibilities of using *in-situ* XAS techniques to probe the individual components in terms of the structural, electronic and the corrosion characteristics of individual alloying elements. This investigation has shown that substitution of Ni and La by Sn and Ce respectively results in changes in the lattice parameters (both Ni-Ni and Ni-La distances) as well as partial filling of the Ni *d* states or lattice distortions causing changes in the coordination symmetry. There was also evidence indicating increase in the number of empty La *d* states. This study also indicated that electrochemical charge and discharge cycles result in Ni corrosion. There was also evidence indicating the ability of Ce to impart corrosion resistance when used as a substituent for La.

This investigation therefore aims to investigate the effect of Ce composition as a substituent for La in a series of metal hydride alloys where the B component remained unchanged. The composition of component B ($Ni_{3.55}Co_{0.75}Mn_{0.4}Al_{0.3}$) was based on those commonly used as AB_5 battery electrodes. Besides these, alloys containing Mm (both synthetic as well as those commercially available prepared from Bastnasite ore) as component A were also used. The principle effort therefore was to investigate the effect of Ce composition in terms of corrosion characteristics of individual alloying components, primarily the Ni.

Experimental

The alloy compositions were LaB_5, $La_{0.8}Ce_{0.2}B_5$, $La_{0.5}Ce_{0.5}B_5$, $La_{0.25}Ce_{0.75}B_5$ and MmB_5 (both synthetic and commercial) where B_5 is $Ni_{3.55}Co_{0.75}Mn_{0.4}Al_{0.3}$. The composition of the synthetic Mm alloy was chosen to be (in atom%) 26% La, 52% Ce, 16% Nd and 6 % Pr. All the alloys were prepared using the arc melting technique and were annealed at 1173°K for 3 days. The details of the preparation conditions used together with the methodology for determination of the P-C-T isotherms, the molar volume of hydrogen in the hydride phase and the X-ray diffraction analysis is given elsewhere (8). Electrodes prepared from a portion of each alloy (73 mg) were subjected to electrochemical cycling using a computer controlled battery cycler (Arbin Corp., College Station, Texas). The charging rate used was 10 mA for 3 hours (2.5 hours for alloys possessing below 300 mAh/gm capacity). The cutoff voltage for the discharge cycle was -0.7 V vs. Hg/HgO reference electrode. The electrode composition used for these tests were in the weight ratio of 17% Teflon, 33% carbon black (Vulcan XC 72) and 50 % alloy. All electrochemical cycling measurements were conducted in a flooded vented cell in 6 M KOH electrolyte. Details of the electrode preparation and testing are given elsewhere (7-9). After 100 cycles the electrode material was removed from the current collector, washed with deionized water to remove KOH and ultrasonically dispersed in acetone. After drying, these material were mixed with BN and pressed into pellets for *ex-situ* XAS studies. The electrodes for the XAS measurements were thin discs (0.25 mm thick and 19 mm in diameter) that comprised of the alloy, carbon black (Vulcan XC-72), vitreous carbon fibers and a polyvinylidine fluoride binder. They were prepared using a standard vacuum table paper making technique (10). Prior to electrode fabrication, all the alloys were activated by subjecting each to several hydriding-

dehydriding cycles in the Sievert's apparatus. This produces a fine powder that eliminates thickness effects in the EXAFS and avoids the need for an electrochemical activation procedure. For detailed accounts of the activation procedure see refs., 11-12. The metal hydride electrodes for the *in-situ* studies were charged at a constant current of 3mA for 7 hours and discharged at a current of 5mA to a potential of -0.7 V vs. Hg/HgO reference electrode. The charging rate allowed for considerable overcharge because the electrodes contained only ≈ 50 mgs of the alloy. XAS scans for the hydrided samples were run after subjecting the electrodes for five charge discharge cycles and were conducted within 30 minutes of termination of charge.

The X-ray absorption spectroscopic (XAS) measurements were conducted at the Beam Lines X23A2 and X11A at the National Synchrotron Light Source (NSLS). Details of the monochromator design, detuning, and energy resolution of the respective Beam Lines are given in detail elsewhere (10, 13-14). XAS measurements were made in the transmission mode, at the La L_3, Ni K and Ce L_3 edges, before and after electrochemical cycling (100 times) and as a function of electrochemical charging. The data acquisition for XAS comprised of three ionization detectors (incidence I_o, transmittance I_t, Reference I_{ref}). The reference channel was primarily for internal calibration of the edge positions and was used in conjunction with pure foils or oxide samples of the respective elements. For the Ni K edge pure N_2 was used in all the chambers, while for the La/Ce L_3 edges a mixture of 80%He and 20%N_2 was used in the incidence chamber while passing pure N_2 in the transmittance and reference chambers. The data analysis package used for the XANES analysis was the University of Washington analysis program (15). The data analysis was done according to procedures described in detail elsewhere (10,13-14,16-17). The EXAFS data analysis used computer algorithms developed by Koningberger and coworkers (15-17). The Fourier filtering and analysis of the EXAFS spectra were conducted according to procedure described in detail elsewhere (10,13-14).

Results and Discussion

X-ray Diffraction and Electrochemical Characterization: Table 1 shows the results of electrochemical and X-ray diffraction analysis. As evident from these results, addition of Ce causes a significant lowering in capacity loss with cycling. Comparison of the cell volume expansion due to hydriding for LaB_5 and $La_{0.8}Ce_{0.2}B_5$ shows similar behavior, which suggests that corrosion resistance imparted due to addition of Ce cannot be simply related to the extent of lattice expansion and contraction as suggested Willems and Buschow (5). As pointed out by Adzic et al., (this conference, (8)), addition of Ce results in higher initial capacity and hence an increase in the number of hydrogen atoms per unit cell. However, as shown in ref. (8), further increase in the Ce composition (beyond 0.2) causes a decrease in the cell volume (due to the smaller size of Ce) which results in higher hydrogen plateau pressure and hence lower charging efficiencies. These are manifested in lower initial capacity and number of hydrogen atoms per unit cell. As a result, the volume expansion due to the hydriding process is lower and this could be a further contributing factor in lower capacity loss, with higher Ce content. The MmB_5 prepared using commercially available Mm had the lowest capacity loss, even less than that for the synthetically prepared analogue. This behavior could be partly explained on the basis of lower cell volume and more importantly lower cell volume expansion as a consequence of

hydriding as compared to the synthetic analogue. Similar electrochemical characteristics (capacity loss, initial capacity number of hydrogen atoms per unit cell etc.) for both synthetic MmB_5 and $La_{0.5}Ce_{0.5}B_5$, both of which possess similar Ce content (~50 atom%) implies that Ce is the prime contributor to corrosion resistance.

XAS results at the Ni K edge: Figure 1 shows the normalized Ni K edge XANES spectra for dry uncycled LaB_5, $La_xCe_{1-x}B_5$ (X=0.8, 0.5 and 0.25) and MmB_5. The XANES for all the electrodes exhibit a small pre-edge peak which can be ascribed to *p-d* hybridization, allowing transitions into the empty 3*d* states of Ni. As shown previously (6-7) such mixing of *p-d* states is expected, based on the hexagonal symmetry of the lattice. However as shown in figure 1 there is no effect on the pre-edge peak as a function of Ce composition, implying minimal distortions in lattice symmetry due to incorporation of Ce. Figure 2 shows the normalized Ni K edge XANES spectra for LaB_5 before and after electrochemical cycling (100 times) together with that of a dry β-$Ni(OH)_2$ electrode. Appearance of a white line for the cycled LaB_5 electrode indicates corrosion of the Ni surface. Comparison of the area under this peak with that for the β-$Ni(OH)_2$ was used to estimate the degree of corrosion. It indicates that 18% of the Ni has corroded (Table 2). Figure 3 compares the white lines for LaB_5 and $La_{0.8}Ce_{0.2}B_5$ after 100 cycles with that for a dry β-$Ni(OH)_2$ electrode. As evident from this figure, the addition of Ce, significantly lowers the Ni corrosion to 8% after 100 cycles (Table 2). Figure 4 shows a similar comparison of the XANES for uncharged dry MmB_5 electrode and an electrode after 100 cycles (both synthetic and commercial). The lack of white line indicates that there was almost no corrosion of the MmB_5 prepared from commercially available Mm ore. Compared to this, the synthetically prepared sample exhibited slightly higher Ni corrosion. As mentioned previously, this difference could be partly explained on the basis of lower lattice expansion in the case of the commercial Mm sample. The extent of Ni corrosion determined from comparison of the white line in the Ni K edge for the cycled MmB_5 samples are given in Table 2. These differences in the Ni corrosion can also be observed in the EXAFS region at the Ni K edge. Figure 5 shows the Fourier transforms of the EXAFS at the Ni K edge for LaB_5 before and after 100 cycles. The main peak centered around 2 Å contains contributions from Ni-Ni interactions from both the basal plane (plane containing both A and B components) and those in between the basal planes containing exclusively the B component. Besides these there are the smaller interaction from Ni-La and Ni-M (where M denotes all the Ni substituents). Comparison of the cycled and uncycled spectra shows formation of peaks around 1.5 Å for the cycled sample and a consequent lowering of the Ni-Ni interactions which could be accounted for, due to the formation of nickel oxides on the cycled electrodes. The absence of these oxides on the uncycled electrodes shows that no nickel oxidation occured in preparing these alloy electrodes. Figure 6 show a similar comparison of the Fourier transform of the Ni K edge EXAFS for $La_{0.8}Ce_{0.2}B_5$. This figure shows evidence for the formation of oxides on the Ni surface on the cycled electrode and its absence in the uncycled ones. Comparison with similar spectra obtained for LaB_5 shows that the extent of this oxide formation after 100 cycles was lower in the sample containing Ce.

XANES Results at the Ce L_3 edge: Figure 7 shows the XANES spectra at the Ce L_3 edge for $La_{0.8}Ce_{0.2}B_5$ as a function of charge and discharge. As evident from this figure, the electrode in its dry uncharged virgin state possesses Ce in a mixed +3/+4 valence state. This is in agreement

with previous results on intermettalic alloys containing Ce (18-19). There is however a change in the oxidation state of Ce to +3 state as a result of hydriding. This is consistent with previous results of Garcia *et. al.,* which involved the $CeRu_2$ and $CeFe_2$ alloys, with hydriding conducted in the gas phase (18). The effect of discharge, is reversion to the mixed +3/+4 state. The increase in the XANES peak at 13 eV in the discharged electrode after 100 cycles indicates some Ce oxidation (fig. 7). Figure 8 shows the analogous XANES spectra for the MmB_5 alloy exhibiting similar effect of oxidation state change during the charging process and its reversion during discharge. The effect of electrochemical cycling however indicated much lower corrosion of the Ce as compared to $La_{0.8}Ce_{0.2}B_5$. This effect was same for both high purity as well as the commercially obtained Mm sample. There also seems to be a direct relation between the magnitude of the white line in the case of Ce in the +3 state (charged electrode) and the hydrogen uptake by the respective alloy. This was confirmed from similar XANES analysis on the other alloy electrodes with different Ce contents ($La_xCe_{1-x}B_5$, with X=0.5 and 0.25).

Ce is a well known corrosion inhibitor for both steel and aluminum (20). The corrosion inhbition properties may be due to the formation of a stable CeO_2 layer. A similar mechanism may be operative in the case of AB_5 hydrides. Further work is neccessary to elucidate the role of Ce in lowering the corrosion rate on cycling.

Conclusions

Based on the results of this study, there is evidence of a direct correlation between the electrochemical stability imparted as a result of addition of Ce (as a substituent to La) and Ni corrosion in the alloy. However, since addition of Ce causes a small degree of lattice contraction (due to the smaller size of Ce as compared to La) its addition beyond ~ 20% causes lowering of the hydrogen uptake and hence electrochemical capacity. In this context it is interesting to note that the synthetic Mm alloy had similar corrosion resistance to the $La_{0.5}Ce_{0.5}B_5$ alloy (both possessing similar Ce content). This was also reflected in the similar extent of Ni corrosion after 100 cycles. The commercial Mm alloy however had a much lower capacity loss and a consequently lower Ni corrosion which could be attributed to the presence of other elements such as Sm, in small amounts as well as the much lower volume expansion during the hydriding process. Results from the XANES analysis at the Ce L_3 edge shows that Ce is present in a mixed +3/+4 state in the unhydrided state and shifts to +3 state during the hydriding step. The formation of a stable Ce rich oxide hydroxide layer on the alloys could account for the improved corrosion resistance of these alloys.

References

(1) J. J. Reilly, in Hydrogen Storage Materials, Batteries and Electrochemistry, (D. A. Corrigan and S. Srinivasan, Eds.,) The Electrochemical Society Inc., 92-5, 24 (1992).

(2) T. Sakai, K. Muta, H. Miyamura, N. Kuriyama and H. Ishikawa, in Hydrogen Storage

Materials, Batteries and Electrochemistry, (D. A. Corrigan and S. Srinivasan, Eds.,) The Electrochemical Society Inc., 92-5, 59 (1992).

(3) J. S. Cantrell, T. A. Beiter and R. C. Bowman Jr., J. Alloys and Compounds 207-208, 372 (1994).

(4) B. V. Ratnakumar, S. Surumpudi, S. Di Stefano, G. Halpert, C. Witham and B. Fultz, 186th Meeting of the Electrochemical Society, Miami Beach, Oct. 9-14, 1994, 94-2, 56 (1994).

(5) J. J. G. Willems and K. H. J. Buschow, J. Less Common Metals 129, 13 (1987).

(6) M. Gupta, L. Schlapbach, Hydrogen in Intermettalic Compounds-I (L. Schlapbach, Ed.,), Topics in Physics Series, Springer Verlag 63, 139 (1988).

(7) S. Mukerjee, J. McBreen, J. J. Reilly, J. R. Johnson, G. Adzic, K. Petrov, M. P. S. Kumar and S. Srinivasan, J. Electrochem. Soc. 142, 2278 (1995).

(8) G. D. Adzic, J. R. Johnson, J. J. Reilly, J. McBreen and S. Mukerjee, J. Electrochem. Soc. (1995), accepted.

(9) K. Petrov, A. A. Rostami, A. Visintin and S. Srinivasan, J. Electrochem. Soc. 141, 1747, (1994).

(10) J. McBreen, W. E. O' Grady, K. I. Pandya, R. W. Hoffman and D. E. Sayers, Langmuir 3, 418 (1987).

(11) J. J. Reilly, in Inorganic Synthesis (S. L. Holt Ed.,) J. Wiley & Sons, New York (1983), p 90.

(12) M. H. Mendelsohn, D. M. Gruen and A. E. Dwight, ibid, p96

(13) S. Mukerjee, J. McBreen, S. Srinivasan and M. P. Soriaga, J. Electrochem. Soc. 142, 1409 (1995).

(14) K. I. Pandya, R. W. Hoffman, J. McBreen and W. E. O' Grady, J. Electrochem. Soc. 137, 383 (1990).

(15) D. E. Sayers, D. A. Bunker, in X-ray Absorption: Principles, Applications Techniques of EXAFS, SEXAFS and XANES, (D. C. Koningsberger and R. Prins, Eds.,) John Wiley & Sons, New York, p 211, (1988).

(16) J. Wong, F. W. Lyttle, R. P. Messner, D. H. Maylotte, Phys. Rev. B. 30, 5596 (1984).

(17) J. B. A. D. van Zon, D. C. Koninsberger, H. F. I. vant' Blik and D. E. Sayers, J. Chem. Phys. 82, 5742 (1985).

(18) J. Garcia, J. Bartolome, M. S. del Rio, Zeitschrift fur Physikalische Chemie Nue Folge, Bd. 163, S 277 (1989).

(19) G. Krill, J. Phys., C8, 907 (1986).

(20) A. J. Davenport, H. S. Isaacs and M. W. Kendig, Corrosion Science 32, 653 (1991).

Table 1

Results of X-ray diffraction and electrochemical characterization as a function of Ce composition.

Composition	n* # of H atoms/Cell	Cell Volume (Å)^3	Initial Capacity mAh/g	Capacity Loss mAh/g cycle
LaB_5	4.8	89.56 (108.56)†	316	0.41
$La_{0.8}Ce_{0.2}B_5$	5.4	88.84 (107.84)†	327	0.21
$La_{0.5}Ce_{0.5}B_5$	4.3	87.33 (104.79)†	278	0.15
$La_{0.25}Ce_{0.75}B_5$	1.3	86.19 (95.16)†	83	-
MmB_5 (synthetic)	4.3	87.39 (101.65)†	283	0.22
MmB_5 (commercial)	3.6	86.27 (97.07)†	231	0.08

* Based on initial electrochemical capacity after activation and one formula unit per unit cell, i.e., AB_5H_n

† Volume measured after gas phase hdyriding.

Table 2

Extent of Ni Corrosion determined from XANES analysis. The degree of corrosion was estimated from the area under the white line.

Alloy Composition	Extent of Ni Corrosion (%)
LaB_5	18
$La_{0.8}Ce_{0.2}B_5$	8
$La_{0.5}Ce_{0.5}B_5$	5
MmB_5 (Synthetic)	4
MmB_5 (Commercial)	2

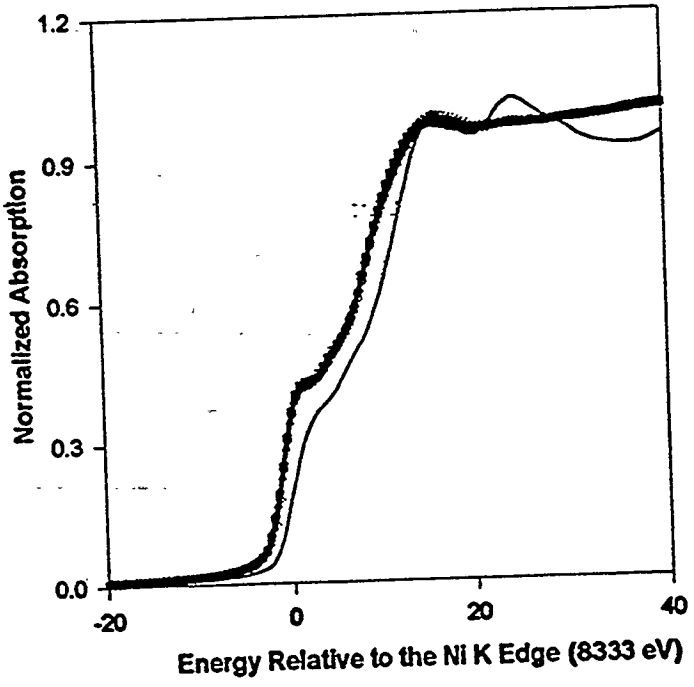

Figure 1. Ni K edge XANES for dry uncharged electrodes. Ni foil (—), LaB_5 (□), $La_{0.8}Ce_{0.2}B_5$ (O), $La_{0.5}Ce_{0.5}B_5$ (▽), $La_{0.25}Ce_{0.75}B_5$ (△) and MmB_5 (◇).

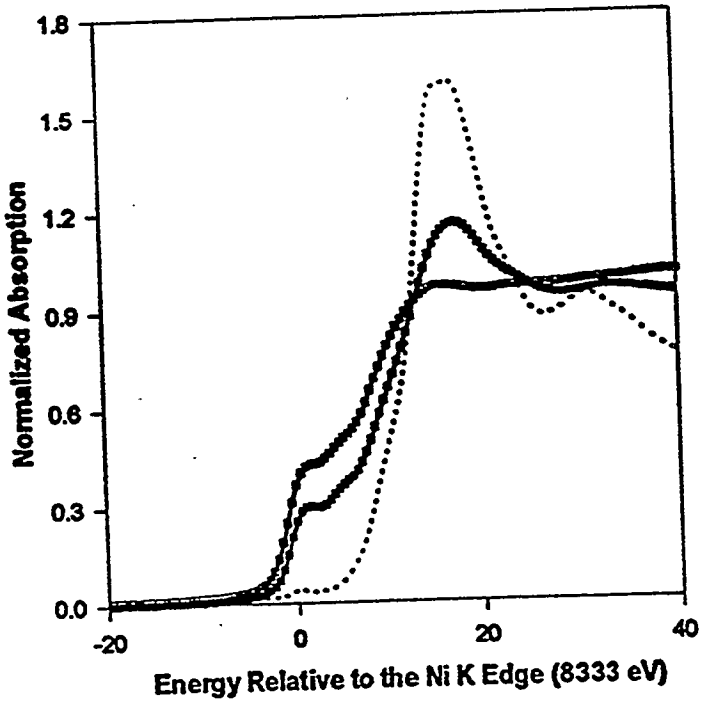

Figure 2. Ni K edge XANES for LaB_5 electrode before and after cycling. $Ni(OH)_2$ (....), Uncycled LaB_5 (□), LaB_5 after 100 cycles (■).

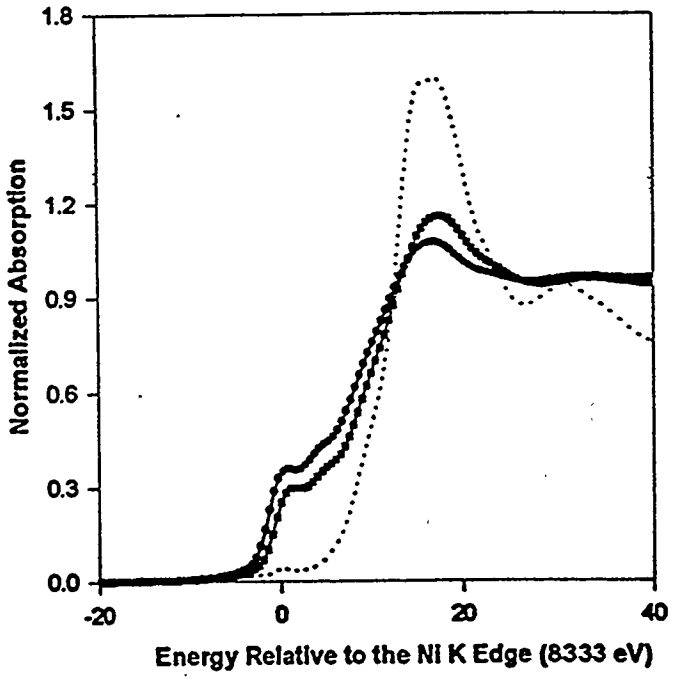

Figure 3. Ni K edge XANES for electrodes after 100 cycles. LaB_5 (■), $La_{0.8}Ce_{0.2}B_5$ (●) and $Ni(OH)_2$ (...).

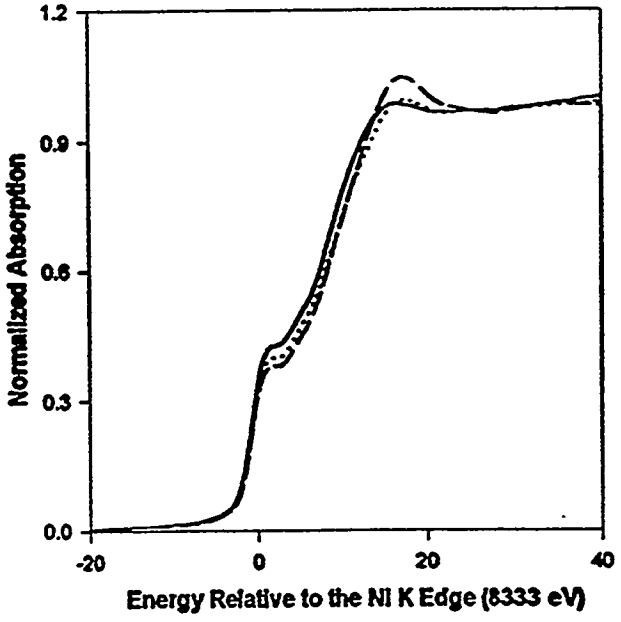

Figure 4. Ni K edge XANES for MmB_5 electrodes (commercial and synthetic) after 100 cycles. MmB_5 (uncycled) (—), MmB_5 (commercial) (...) and MmB_5 (synthetic) (—).

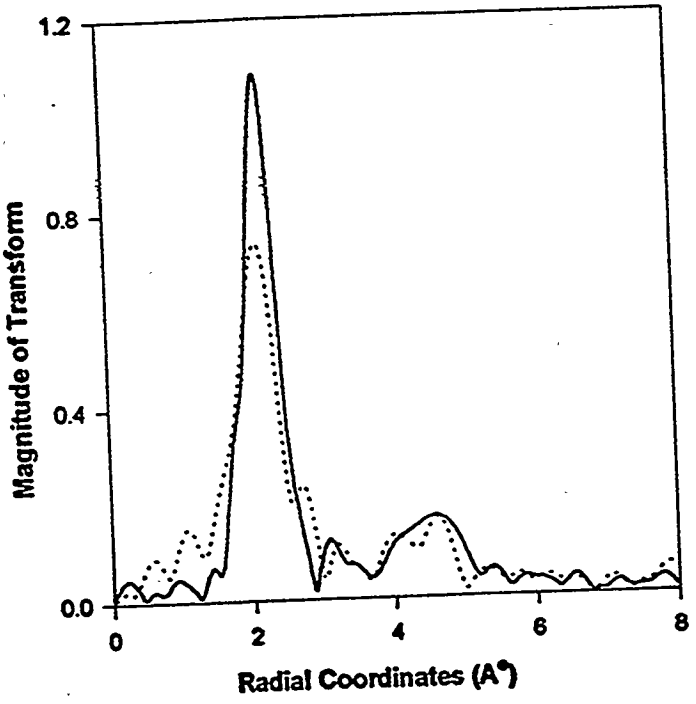

Figure 5. EXAFS at the Ni K edge for LaB_5 electrode before (—) and after 100 cycles (....).

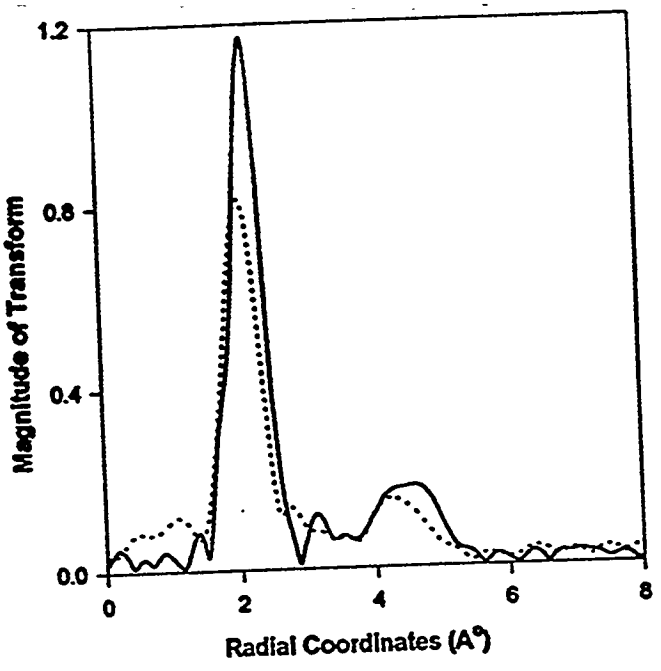

Figure 6. EXAFS at the Ni K edge for $La_{0.8}Ce_{0.2}B_5$ electrode before (—) and after 100 cycles (....).

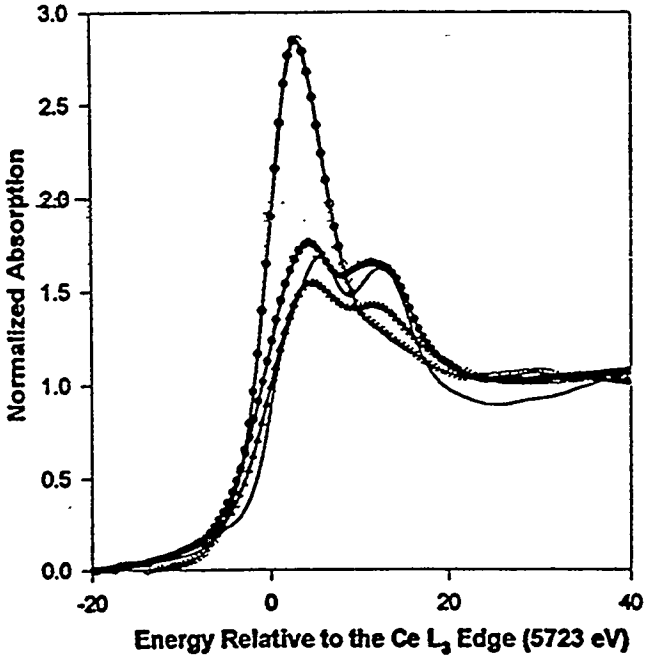

Figure 7. Ce L_3 XANES for $La_{0.8}Ce_{0.2}B_5$ as a function of charge and discharge after 100 cycles. CeO_2 reference standard (—), $La_{0.8}Ce_{0.2}B_5$, dry uncharged (Δ), charged (O) and discharged after 100 cycles (●).

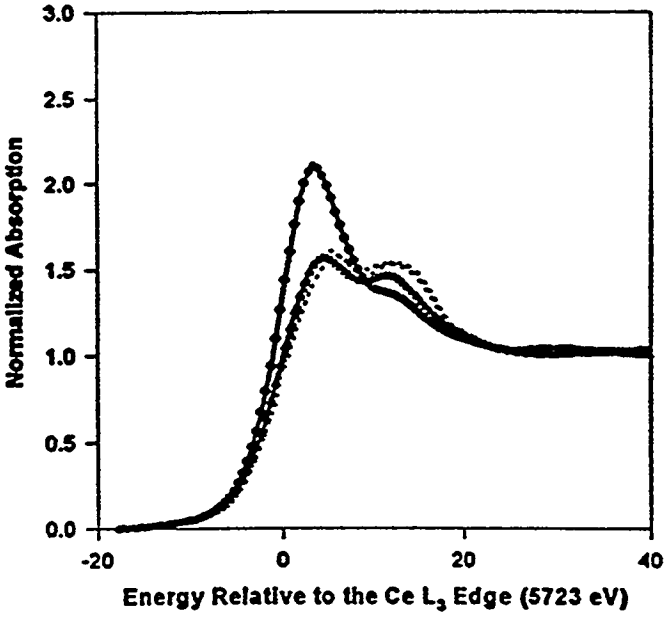

Figure 8. Ce L_3 XANES for MmB_5 as a function of charge and discharge after 100 cycles. MmB_5, dry uncharged (Δ), charged (O) and discharged after 100 cycles (both commercial and synthetic) (...).

4. CORROSION CURRENT MAPS OF AB_5 ELECTRODE SURFACES

W. Zhang, S. Mukerjee, J. McBreen, G. Adzic, J.R. Johnson, J.J. Reilly, S.-M. Huang, H.S. Isaacs, BNL; M.P.S. Kumar and S. Srinivasan,Texas A&M University

Introduction

While certain AB_5 hydrides are attractive as replacements for the cadmium electrode in nickel-cadmium batteries, the paradigm compound of this hydride class, $LaNi_5H_6$ is not suitable because it corrodes rapidly in the battery environment. However, partial substitution of Ni by a variety of metals such as Co, Al, Si etc. has been found to greatly improve its performance as an electrode. This remedy has been attributed primarily to the reduction of the molar volume of hydrogen, V_H, in the hydride phase thereby reducing alloy expansion and contraction during the charge-discharge cycle; this leads to a reduction of the flushing action of the electrolyte through the small pores and fissures of the alloy which are produced in the activation process (1). Consequently corrosion of the electrode is reduced. While the effects of Ni substitution has been widely studied, relatively little effort has focused on the effect of La substitution. This neglect is probably due to the good performance and low cost of mischmetal MmB_5 battery electrodes. However, it has recently been demonstrated that the composition of the rare earth component is also important with respect to electrode life time (2) i.e. the presence of cerium retards corrosion even when allowance is made for alloy expansion and contraction. A possible explanation for this finding lies in the fact that Ce can form a protective oxide film on metal surfaces (Al, mild steel and others) (3). This paper reports on the examination of the surface of two AB_5 metal hydride electrodes using the scanning vibrating electrode technique (SVET). This technique (4) maps, under an open external circuit, the anodic and cathodic current flow on a flat electrode surface in contact with a suitable electrolyte and from which it is possible to infer its resistance to corrosion. The technique is based on the fact that corrosion usually occurs via separate anodic and cathodic sites on the surface. Associated with the corrosion process are currents that go through the electrolyte. The equipotential lines in the electrolyte are orthogonol to the current lines. The vibrating probe senses the changes in potential normal (z axis) to the corroding surface. By rastering the vibrating probe over the surface it is possible to detect anodic and cathodic sites and the current distribution on the surface. The typical area scanned is 3,000 × 3,000 μ with a 100 μ distance between scans along the x and y axes. This gives a total of 900 data points from which the current distribution can be derived. To maximize the penetration of the current lines into the electrolyte it is necessary to use a dilute electrolyte that has a significant resistivity. Accordingly, the electrolyte used was 0.01 M KOH. Two electrodes were examined, one of synthetic mischmetal, i.e., $La_{.26}Ce_{.52}Nd_{.16}Pr_{.06}Ni_{3.55}Co_{.75}Mn_{.4}Al_{.3}$, the other was $LaNi_{3.55}Co_{.75}Mn_{.4}Al_{.3}$; henceforth they shall be referred to as the MmB_5 and LaB_5 electrodes.

Experimental

The alloys were prepared by arc melting after which they were annealed at 1173K for 3 days. Both alloys were single phase as determined by X-ray diffraction. Pressure - composition isotherms were obtained for both alloys and both had plateau pressures below 1 atm. at 298K.

A Ni wire was soldered to a small piece of the ingot alloy sample after which it was mounted in epoxy holder and the exposed surface polished to bright smooth finish with 0.3 μm alumina. The electrode was introduced into a cell with 0.01 M of KOH solution. Current density mapping (4) at open circuit potentials was used to study the corrosion current distribution.

Results and Discussion

The SVET was scanned over a flat alloy in solution. The technique involves the vibrating of a micro reference electrode near the surface. It detects potential gradient as results of current flow in solution between localized anodic and cathodic sites. Figures 1 and 2 show current density maps of the electrode surface. The positive and negative currents indicate where anodic and cathodic reactions are occurring and which are presumed to be caused by corrosion of the alloy at electrode/electrolyte interface. The LaB_5 alloy (Fig. 1) has a rather high corrosion current density with several distinct anodic and cathodic sites. The current density profile for the MmB_5 alloy was significantly lower (Fig. 2). Note that both plots are plotted on the same scale. The results for $La_{0.8}Ce_{0.2}B_5$ were very similar to those found for the MmB_5 electrode. These results are consistent with the results in Section 1 of the Report and give further indication that the presence of cerium retards electrode corrosion (2). Figure 3 shows cyclic voltammograms for LaB_5 and MmB_5 at potentials positive to the hydriding potential. The peaks in the voltammogram for MmB_5 are consistent with a Ce(IV)/Ce(III) redox process on the surface, indicating the presence of Ce on the alloy surface.

Conclusions

The reduced corrosion current in cerium containing electrodes is consistent with previous results (2) where the presence of Ce in a homologous series of AB_5 alloys was demonstrated to have a beneficial effect on electrode lifetime.

References

(1) J. J. G. Willems, Philips Journal of Research 39-1, 1 (1984).

(2) G. D. Adzic, J. R. Johnson, S. Mukerjee, J. McBreen, J. J. Reilly, M. P. S. Kumar, W. Zhang and S. Srinivasan, Proceedings Hydrogen and Metal Hydride Batteries, P. D. Bennett and T. Sakai Eds., 186th Meeting of the Electrochemical Society, Miami Beach, Florida, Oct. 9-14, (1994).

(3) A. J. Davenport, H. S. Isaacs, and M. W. Kendig, Corrosion Science 32, 653 (1991).

(4) H. S. Isaacs, Corrosion Science 28-6, 547 (1988).

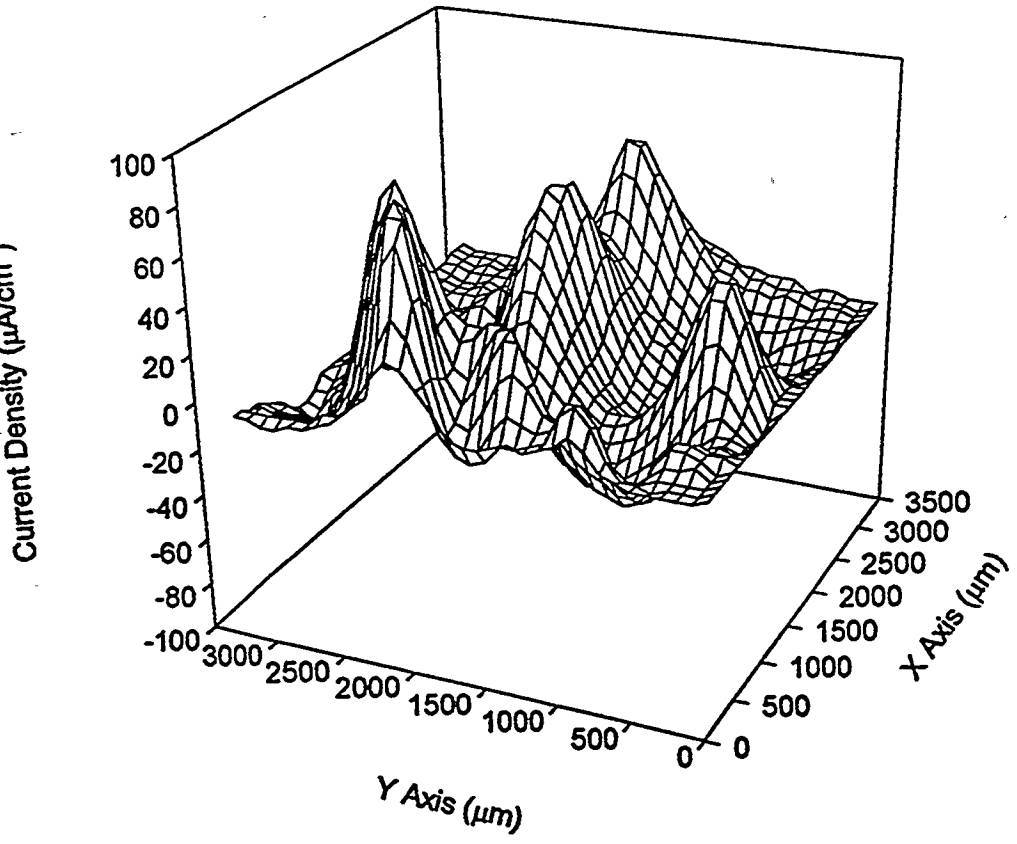

Fig. 1. 3-D plot of the normal current density distribution for LaB_5 ingot electrode at time of about 100 min. immersed in 0.01M KOH.

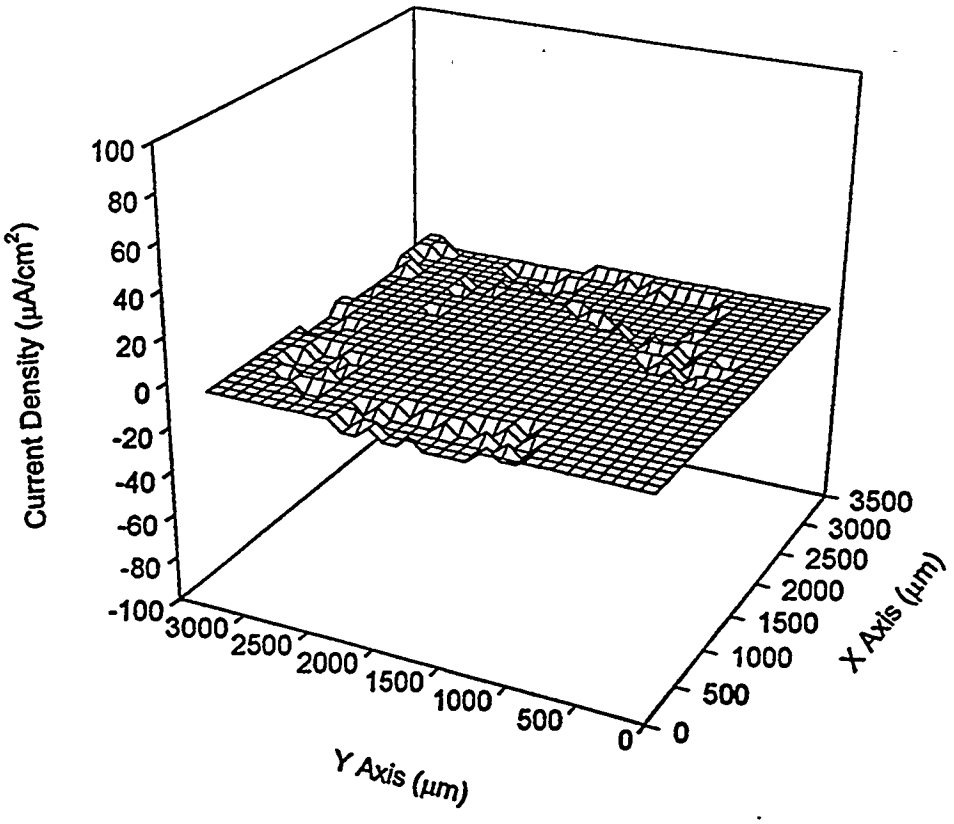

Fig. 2. 3-D plot of the normal current density distribution for MmB_5 ingot electrode at time of 100 min. immersed in 0.01M KOH.

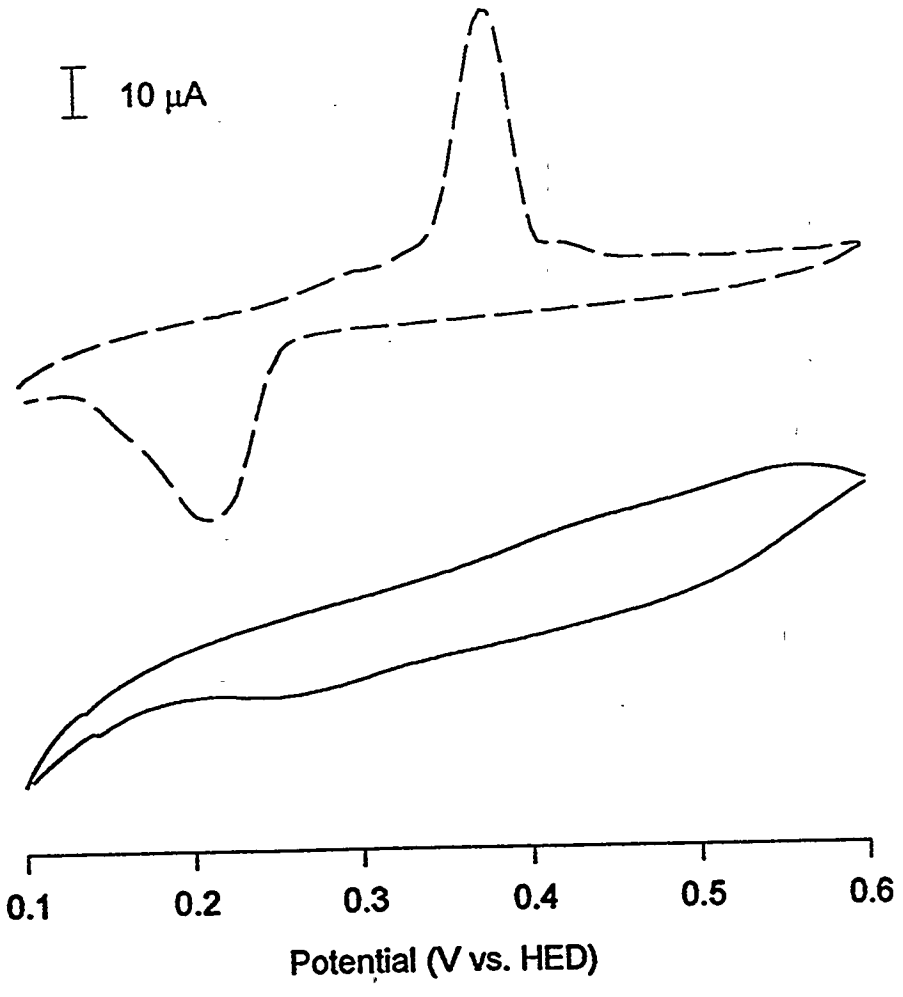

Fig. 3 Cyclic voltammetry plots of LaB_5 (—) and MmB_5 (- -) in 6M KOH solution at scanning rate of 1 mV/s.